Selina Kayla Linnemann

Functional morphology of diatom frustules and their potential for the development of bio-inspired stiffening structures

UNIVERSIDADE DO ALGARVE

Faculdade de Ciências e Tecnologia

2023

Selina Kayla Linnemann

Functional morphology of diatom frustules and their potential for the development of bio-inspired stiffening structures

Mestrado em Biologia Marinha

Supervisors:

Dr. João Miguel Sousa da Silva

Co-supervisor

Dr. Christian Hamm-Dubischar

UNIVERSIDADE DO ALGARVE

Faculdade de Ciências e Tecnologia

2023

Abstract

The intricate and highly complex morphologies of diatom frustules have long captured the attention of biomimetic researchers, promoting innovation in engineering solutions. This study investigates the potential of diatom-inspired surface stiffeners to determine whether the introduced innovative strategy is a viable alternative for addressing engineering challenges demanding enhanced stiffness. By merging principles from both biology and engineering, this interdisciplinary study focuses on the computer-aided generation of stress-adaptive structures aimed at optimising bending stiffness. The study serves as a framework for innovation by approaching scientific questions from a new perspective, enabling the application of biomimetic principles to formulate novel scientific methods. The biomimetic approach involves identifying a biological analogy for technical challenges, here exemplified by the resilient diatom frustules. Through a comprehensive microscopical analysis consisting of light microscopy, confocal laser scanning microscopy, and scanning electron microscopy, morphological characteristics were identified to derive geometrical principles from the observations. The abstracted principles were then applied to a reference model utilizing computer-aided methods and simulated to analyse their mechanical behaviour under load-bearing conditions. Afterwards, the models were compared against a conventional engineering approach. A total of 17 diatom genera were identified, exhibiting structural elements such as combs, ribs, and hierarchical layers. The most promising biomimetic approach was successfully automated, extending its applicability to non-planar surfaces and diverse boundary conditions. It yielded notable improvement in bending stiffness, which manifests a decrease of displacement by approximately 93 % in comparison to the reference model with an equivalent total mass. Nonetheless, for the specific load case considered, the engineering approach yielded the least displacement. Although certain applications may favour conventional methods, diatom-inspired stress-adaptive designs appear promising for scenarios subjected to varying stresses, necessitating lightweight and robust solutions. The applications of diatom-inspired stiffening structures extend across a range of fields, including aerospace engineering, medical devices, and civil engineering.

Keywords:

Functional morphology, diatom frustules, biomimetics, surface stiffening

Resumo

As morfologias altamente complexas e intrincadas das frústulas de diatomáceas têm sido um tema fascinante na pesquisa biomimética, inspirando o desenvolvimento de soluções de engenharia inovadoras. Na natureza, as diatomáceas enfrentam diversos obstáculos mecânicos que afetam a sua sobrevivência. A parede celular silicificada, conhecida como frústula, é uma estrutura multifuncional que desempenha vários papéis vitais, incluindo proteção contra ataques de predadores. As diatomáceas pelágicas, em particular, superam com sucesso o desafio de manter simultaneamente a resistência mecânica e as características de leveza e baixa densidade que lhes permitem permanecer na parte superior da coluna de água, onde recebem a luz necessária à fotossíntese. Essa combinação torna-as extremamente interessantes para aplicações tecnológicas, nomeadamente nos campos da engenharia leve, onde engenheiros e cientistas procuram soluções para reduzir o peso, mantendo simultaneamente o desempenho mecânico. Supõe-se que estruturas leves inspiradas em diatomáceas possam oferecer um aumento na rigidez de superfícies de forma mais eficiente comparativamente com os métodos de engenharia convencionais. Este estudo investiga o potencial de endurecedores de superfície inspirados em diatomáceas para determinar se as estratégias inovadoras introduzidas são uma alternativa viável para abordar desafios de engenharia que exigem maior rigidez. Ao combinar princípios da biologia e da engenharia, este estudo interdisciplinar concentra-se na geração assistida por computador de estruturas adaptadas ao stress, visando otimizar a resistência à flexão. Este trabalho serve ainda como um quadro de inovação, abordando questões científicas a partir de uma nova perspectiva e permitindo a aplicação de princípios biomiméticos para formular novos métodos de engenharia.

O estudo segue uma abordagem biomimética, que envolve a identificação de uma analogia biológica para um determinado desafio técnico, neste caso, o desafio do endurecimento de superfícies, baseando-se nas frústulas de diatomáceas como uma analogia biológica, seguido por uma abstração dos princípios e transferência para uma aplicação técnica. O processo foi estruturado em três partes principais. A primeira parte envolveu uma análise microscópica abrangente, incluindo microscopia de luz, microscopia confocal de varrimento a laser e microscopia eletrónica de varrimento. Esta análise permitiu a identificação de características morfológicas e a derivação de princípios geométricos a partir das observações. A segunda parte do estudo incluiu o desenvolvimento de estruturas de endurecimento para uma aplicação técnica generalizada. Esta fase começou com a configuração de um modelo computacional de uma placa para servir como modelo de referência, seguido pela definição de casos de carga e condições de contorno. Várias abordagens bioinspiradas foram exploradas, utilizando uma abordagem biomimética, incluindo uma abordagem de nervuras, uma abordagem de pentes e uma abordagem combinada que utilizava estruturas de sanduíche adaptáveis ao stress. Além disso, uma abordagem de engenharia na forma de otimização de espessura foi também realizada. Estes modelos foram então simulados para analisar o comportamento mecânico sob condições de carga, e subsequentemente comparados com a abordagem de engenharia convencional. O último segmento do estudo envolveu a variação das condições de contorno tanto para a abordagem bioinspirada mais promissora como para a abordagem de engenharia, com o objetivo de testar a robustez do fluxo de trabalho. Isso foi alcançado através da seleção de um modelo de referência e configuração de carga inovadora.

Um total de 17 géneros de diatomáceas foram identificados através de microscopia confocal a laser e microscopia eletrônica de varrimento. As principais características estruturais observadas nas frústulas incluiam pentes com uniformidade variável e gradientes de tamanho, nervuras e suportes, além de camadas hierárquicas. Em geral, todos os modelos com estruturas de endurecimento inspiradas em diatomáceas consistentemente superaram a estratégia simplista de espessar uniformemente a placa de referência. A rigidez dos modelos foi aprimorada com sucesso ao minimizar o deslocamento dos modelos sob carga. Muitas características morfológicas das frústulas, como pentes, nervuras e estruturas de sanduíche, foram examinadas sob uma perspectiva mecânica. Um princípio discernível foi o aprimoramento do segundo momento de áreas. Quanto mais material estiver localizado na distância máxima possível do centróide da seção transversal, como numa estrutura de sanduíche, ou através do aumento das alturas das nervuras, maior será o segundo momento de área e a rigidez subsequente. Os princípios abstraídos relacionados com o aumento do segundo momento de área mostraram-se confiáveis para aprimorar a rigidez da superfície.

A abordagem biomimética mais promissora foi o desenvolvimento de um modelo adaptado ao stress, cujo padrão de pentes e estrutura de sanduíche foram adaptados ao campo de stress do modelo em termos de disposição, altura e espessura. O fluxo de

trabalho para criar essa abordagem foi automatizado com sucesso, ampliando a sua aplicabilidade a superfícies não planas e a diversas condições de contorno. Assim, esse modelo resultou em estruturas adaptadas a uma distribuição específica de stress de um cenário fornecido, definindo apenas os seus parâmetros, como as condições de contorno. Este modelo apresentou um notável aumento na resistência à flexão, o que resultou numa diminuição do deslocamento de aproximadamente 93 % em comparação com o modelo de referência, com uma massa total equivalente. Uma abordagem alternativa, incluindo um design hierárquico com nervuras principais e pentes conectores, reduziu o deslocamento em 77 %. No entanto, para o caso de carga específico considerado, a abordagem de engenharia apresentou o menor deslocamento, com uma diminuição de 97 %. Este resultado levanta a questão de porquê uma distribuição de material simplesmente otimizada em espessura não é comumente observada nas frústulas de diatomáceas. Embora esse princípio esteja presente em certas estruturas naturais, como árvores ou ossos, que rotineiramente enfrentam forças consistentes, a maioria dos organismos vivos são generalistas e precisam ser resistentes a uma variedade de diferentes casos de carga. As diatomáceas são um exemplo disso, dado que necessitam de gerir uma série de factores distintos de stress, introduzidos por diversos predadores. Problemas técnicos em muitos casos enfrentam um conjunto muito específico de forças, como as apresentadas neste estudo, que diferem das forças complexas e variadas encontradas na natureza e em cenários do mundo real. Isso implica que a otimização de espessura pode ser mais aplicável para casos de carga específicos e consistentes, pois é ajustada especificamente a esse conjunto de forças. No entanto, a eficácia da otimização de espessura diminui quando confrontada com diferentes dinâmicas de força. A abordagem de sanduíche adaptável ao stress, como demonstrado, emerge como uma solução altamente promissora, com potencial para aprimoramento adicional. Portanto, pode-se supor que os endurecedores de superfície biomiméticos sejam mais adequados para casos de carga complexos, por apresentarem um design mais robusto e versátil, que exibe resistência a uma gama ampla de casos de carga.

Os designs adaptativos inspirados em diatomáceas apresentam-se promissores para cenários sujeitos a diferentes tipos de stress, exigindo soluções leves e robustas. As aplicações de estruturas de endurecimento adaptativas inspiradas em diatomáceas estendem-se por uma variedade de campos, incluindo engenharia aeroespacial, dispositivos médicos e engenharia civil. As estruturas de endurecimento adaptativas

podem ainda ser aplicadas em dispositivos médicos, como próteses, onde uma elevada robustez é necessária. O design paramétrico permitiria a criação rápida de designs personalizados, adaptados de maneira ideal às características físicas de cada paciente. Em resumo, as descobertas deste estudo evidenciam o potencial notável das frústulas de diatomáceas como inspiração para a engenharia biomimética. Este estudo contribui também para o contínuo debate sobre soluções inspiradas na natureza e convida a uma exploração mais aprofundada de métodos interdisciplinares.

Palavras da chave:

Morfologia funcional, frústulas de diatomáceas, biomimética, endurecimento de superfície

Functional morphology of diatom frustules and their potential for the development of bio-inspired stiffening structures

Declaração de autoria de trabalho

Declaro ser a autora deste trabalho, que é original e inédito. Autores e trabalhos consultados estão devidamente citados no texto e constam da listagem de referências incluída

Faro, _________________ signatura _____________________

List of abbreviations

1D	One dimensional
2D	Two dimensional
3D	Three dimensional
AWI	Alfred-Wegener-Institute, Helmholtz Centre for Polar and Marine Research
CAD	Computer-aided design
CAE	Computer-aided engineering
CLSM	Confocal laser scanning microscopy
FE	Finite element
FEA	Finite element analysis
FEM	Finite Element Method
QUAD4	Four-noded rectangular surface element
SEI	Secondary electron imaging
SEM	Scanning electron microscopy
SF	Stress field
SIMP	Solid Isotropic Material with Penalization, Algorithm for computer-aided topology optimisation
TRIA3	Three-noded triangular surface element

Symbol	**Unit**	**Description**
A	mm^2	Area
A_r	%	Remaining Area regarding the initial area
c_s	mm	Comb size
d_c	mm	Global distance value
d_o	mm	Offset distance
E	MPa	Young’s modulus
F	kN	Force
h_c	mm	Rib height

I	mm^4	Second moment of area
K_B	N mm^2	Bending stiffness
l_e	mm	Average element size
m_t	kg	Total mass
P_m	-	Midpoint
s_f	-	Scaling factor
t	mm	Thickness
δ_{max}	m	Maximum overall displacement
ρ	kg m^{-3}	Density
ρ_i	kg m^{-3}	Element density
ρ_i^0	kg m^{-3}	Initial element density
ρ_n	kg m^{-3}	Normalised density
σ_{VM}	MPa	Von Mises Stress

Content

1 Introduction

1.1 Diatoms

Diatoms stand out among aquatic organisms for their remarkable diversity. Estimates reveal that hundreds of thousands of species exist (Kooistra et al., 2007), successfully occupying global habitats (Round et al., 1990). Their high abundance and photosynthetic capacity make them one of the main primary producers in aquatic ecosystems, providing the base of the food chain for a vast number of aquatic organisms (Renaudie, 2016). Diatoms are unicellular eukaryotes that belong to the phylum Bacillariophyta (Round et al., 1990). They can be found in marine and freshwater environments and thrive in a variety of ecological niches, ranging from polar regions to tropical waters. They exist in drifting communities and epiphytical forms, living either freely in the water column or attached to surfaces such as rocks, sediment, or aquatic flora and fauna.

The diverse habitats that diatoms occupy have contributed to the evolution of a wide range of shapes and sizes, reflecting their ability to adapt to different ecological niches. The high degree of biodiversity is evident in the distinct morphologies of diatom frustules, except for a few cryptic species (e.g., Round et al., 1990; Young & Geisen, 2002). Their silicified cell walls offer intricate structures and ornamental patterns, which made them a target of interest for artists, scientists, and engineers alike. The size of these structures ranges from nano to microscale, which makes microscopy an indispensable tool for their investigation (Kooistra & Pohl, 2015). In the early days of studying diatoms, researchers had to rely primarily on light microscopy for this exploration, such as Ernst Haeckel (2012) for his scientific illustrations in art forms in nature first published in 1904 (Figure 1.1). However, the limitations of light microscopy became evident as it could only provide a limited level of detail and resolution (Kooistra & Pohl, 2015). With the advance in imaging techniques, bringing methods such as electron microscopy, a new era unfolded in diatom research. Especially electron microscopy allows us to examine diatoms at much higher magnifications, revealing previously unseen details and providing a deeper understanding of their morphology.

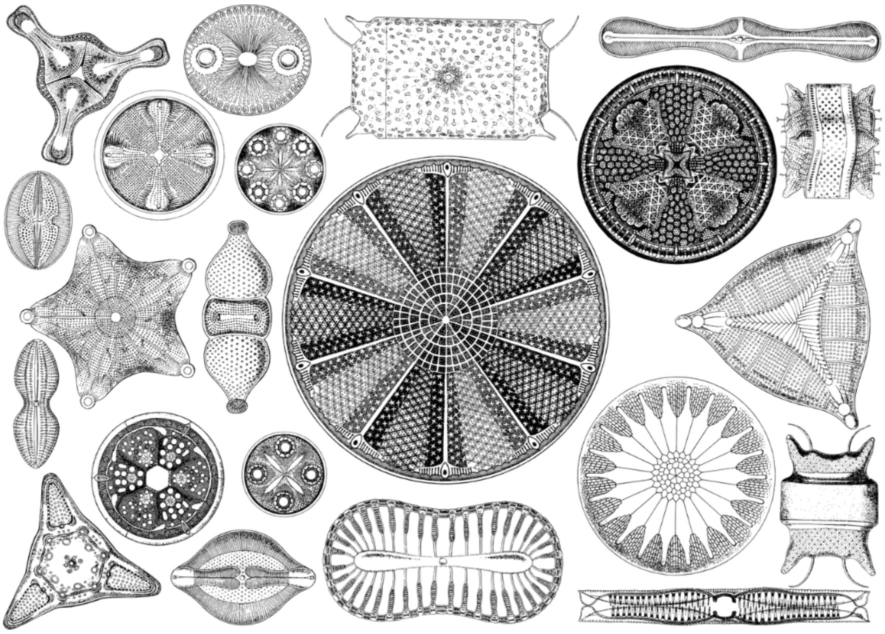

Figure 1.1. Diatoms by Ernst Haeckel in “Art forms in Nature” 1904 (Pixabay. https://pixabay.com/vectors/diatoms-nature-wildlife-geometry-4906058/)

1.2 Ecology and morphology of diatoms

With the use of advanced microscopic methods, habitat and species-specific features could be revealed. All diatoms consist of a nucleus, cytoplasm, plasma membrane, and cell wall (Round et al., 1990). They can be unicellular or colonial, existing for example in chain-like communities. The species-specific morphology of the cell walls allows their taxonomic classification. Based on the shape of their frustules Round et al. (1990), suggested the classification of diatoms into two broad groups, Centrales (centric diatoms) and Pennales (pennate diatoms). Centric diatoms are typically circular or elliptical and are radially symmetric, meaning they have symmetry around a central axis. Pennate diatoms, on the other hand, are elongated and bilaterally symmetric, with the symmetry plane running along the long axis of the cell. In marine habitats, Centric diatoms are more commonly found in marine planktonic communities, while pennate diatoms are associated with microphytobenthos (McLaughlin, 2012; de Tommasi et al., 2017)). They are prevailing in epipelic and benthic environments, such as aquatic plants and sediments. They are also associated with warmer waters and are more common in fresh waters, such as lakes, rivers, and streams. Another possible classification can be made based on features of their frustules.

Centric diatoms can be further divided based on the pattern of their valves. Some diatoms have a circular valve with a raised centre, while others have a more complex pattern of ridges and grooves (McLaughlin, 2012; Round et al., 1990). Pennate diatoms can be classified into subgroups based on the absence or presence of a raphe: araphid, monoraphid and biraphid. Araphid diatoms have no central raphe, which is a groove that runs along the valve, while monoraphid diatoms have a single, central raphe, and biraphid exhibit a raphe on both valves. They can then be divided into groups based on the position of the raphe, which can be either central or eccentric. Eccentric raphe diatoms have the raphe located closer to one end of the cell than the other or positioned along the perimeter of the valve, which gives them a distinct shape. It is important to note that this is only one suggested classification method, over the decades many classification schemes for diatoms have been presented which are based on different, mainly morphological, criteria (McLaughlin, 2012).

The frustule of diatoms can range in size from about 2 µm to 2 mm in length or diameter (De Tommasi et al., 2017; Kakizaki et al., 2011) and is composed of two box-like parts and a set of bands connecting the former (Figure 1.2). The epitheca is the upper part of the frustule consisting of the epivalve and a band, the epigirdle (McLaughlin, 2012). The hypotheca is the set of the lower slightly smaller valve with the hypogirdle. These parts fit together to enclose the cell and exist in a variety of different sizes and shapes from flattened cylinders to complex twisted geometries. The set of girdle bands is typically two, but some species exhibit a larger number (Goessling et al. 2019). A closer look at the valve reveals a hierarchical structure.

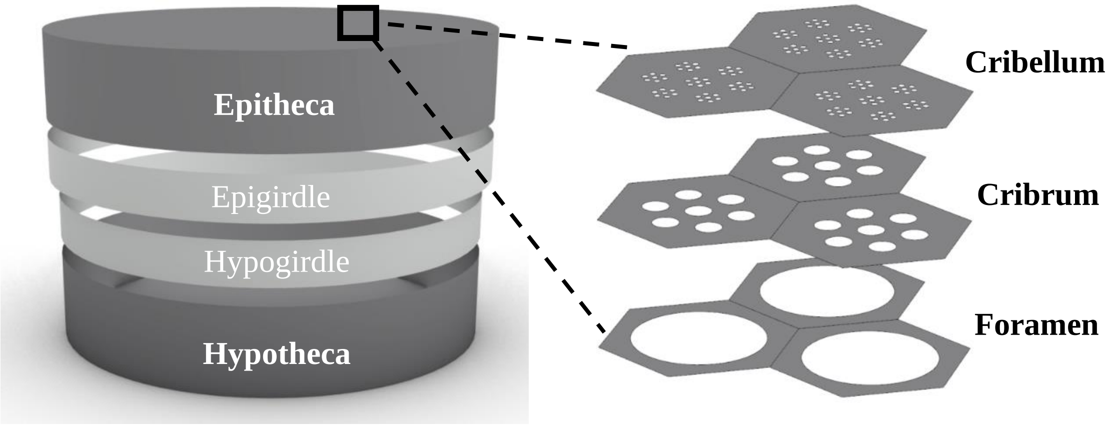

Figure 1.2. Abstracted model of the parts of a centric diatom frustule and detailed cross-section of a generalized valve with three different layers.

The valve of the centric diatoms is typically more complex than that of a pennate diatom (Aguirre et al., 2018). The frustule consists of different layers, which can vary depending on the species. In many centric diatoms, the valve is composed of three overlapping layers with different pore sizes (Aguirre et al., 2018; Mcheik et al., 2018). The external side is called the cribrum, which includes a thin membrane with smaller porous silica connections called cribellum, exemplifying a perforated plate (Figure 1.2). The third and internal layer is called the foramen. The cribrum is connected to the foramen by silica walls named areolae. In addition to these structures, the valves can exhibit a variety of chambers, struts, ribs, crests, and troughs. A description of these structures and their corresponding terms can be found in A.1. The dimensions, shapes, and patterns of these pores are species- and layer-specific (De Tommasi et al., 2017).

The valves and the girdle bands are made of amorphous, hydrated silica and exhibit different surface defects (Gebeshuber & Crawford, 2006; Qin et al., 2008). The silica is colloidal and deposited in micro- and nanopatterns (Iler, 1979). For the synthesis of the cell walls diatoms depend on silica biogenesis, acquiring silicic acid from its environment. Additionally, to the silicified cell walls, a layer of extracellular polysaccharide polymer networks covers the frustule of most species, fulfilling different purposes on cellular levels and in the environment (Svetličić et al., 2013).

1.3 Function of diatom frustules

The intricate morphology of diatoms and the unique composition of their frustule lay the foundation for their multifunctionality (De Tommasi et al., 2017). A variety of adaptive roles have been suggested for the frustule, including protection and defence against attacks, nutrient exchange, support of the vacuole, light harvesting, protection against UV radiation and buoyancy control. In recent studies, the defensive role has gained interest as the main function of the frustule (e.g., Hamm et al., 2003; Pondaven et al., 2007), but experimental evidence and studies of the function of the frustule are scarce and leave room for speculations (Pančić et al., 2019). A few of the previously mentioned functions shall be described in more detail.

Protection and Defence Against Attacks

As highly abundant primary producers, diatoms are extensively targeted by a range of organisms (Hamm et al., 2003). Pathogens, parasitoids and predators utilize diverse chemical and mechanical strategies to access their plasma. The latter can involve a variety of herbivores, such as copepods, nematodes, gastropods and Euphausiacea functioning at various scales of size (Hamm, 2005). Consequently, there is a substantial demand for their shells to adapt and enhance specific mechanical properties, given the impact it has on their survival rate (Hamm, 2005). The predators exhibit a wide range of feeding strategies that manifest in numerous types of physical forces acting on the shell, such as point forces and pressure. Nevertheless, diatoms are able to dominate phytoplankton blooms, due to their lower mortality rates when compared to other phytoplanktonic groups (Hamm et al., 2003). According to Hamm and Smetacek (2007), the successful deployment of effective defence mechanisms is critical for survival and maintaining ecological success. The protective silica-based frustule is highly resistant to physical and chemical degradation, making it difficult for organisms to break through and consume the diatom cell.

Evidence in favour of a protective function of the frustule is further given by the fact that its characteristics are “inducible” (Pondaven et al., 2007; Pančić et al., 2019). This implies that they are enhanced or triggered when predators are present, or predator cues are detected. Pondaven et al. (2007) have shown that the degree of shell silicification depends on the environment, with greater amounts of silica found in shells grown in a predatory environment. Silica is very brittle, but relative to its density, the strongest known biological material (Aitken et al., 2016; Pančić et al., 2019). Studies revealed the presence of organic material in the silicified cell walls (Garcia & Buehler, 2010). The combination of an organic damping matrix and stiffening silica results in a highly strong and durable compound.

The structural strength of the frustule is not solely attributed to its material properties but also its architecture (Aitken et al., 2016). When considering pelagic diatoms, a simple thickening of the frustule results in an increased mass, which in turn leads to a faster sinking rate due to the higher density of the material compared to the surrounding seawater (Hamm, 2005; Pondaven et al., 2007). However, as stated by Hamm (2005) especially in the case of pelagic diatoms, it is crucial to remain in the upper water column to carry out photosynthesis. Therefore, the frustule must provide protection while also being lightweight. As a result, the frustules exhibit diverse and complex geometries, arranged in micro- and nanopatterns (Aitken et al., 2016). The high mechanical resilience and the diverse patterns indicate that diatoms are exposed to a vast selective pressure by diverse attacks, and it can be assumed that the shape of the frustule must have an impact on lowering mortality (Hamm, 2005).

Nutrient exchange and light harvesting

While protection of the cell is mentioned as the main purpose of the frustule (De Tommasi et al., 2017), it is not its only function. As photosynthetic organisms, diatoms require a variety of nutrients to survive and grow. The cover of the cell drastically reduces its active surface for nutrient diffusion and uptake (Finkel & Kotrc, 2010). Even with this disadvantage, diatoms exhibit some of the highest rates of growth compared to other types of phytoplankton, when normalised to their cell size (Irwin et al. 2006; Raven & Waite, 2004). This suggests that the surface area of the porous openings in the cell walls offers sufficient space for the necessary number of transporters to maintain elevated levels of nutrient uptake rates (Berg & Purcell, 1977). The frustule is permeable to a variety of small molecules, such as carbon dioxide, oxygen, and nutrients like nitrogen and phosphorus, which are essential for photosynthesis and growth. The size and shape of the pores in the frustule can also influence the types and amounts of nutrients that the diatom can take up and differ depending on environmental conditions.

The silica of the frustule has unique optical properties, similar to those of artificial photonic crystals (De Stefano et al., 2007a). Thus, it can be assumed that valves and girdles may have a crucial function in managing and utilizing light, apart from providing mechanical protection and nutrient accumulation (De Tommasi et al., 2017). The favourable optical properties could potentially increase photosynthetic efficiency in environments where light is limited. Studies state that material combined with intricate structures can enhance light absorption and scattering (e.g., Goessling et al., 2018; De Stefano et al. 2007a, 2007b). The frustule may also act as a lens, focusing light onto the chloroplasts of the diatom cell. Some species are thought to be able to modify their morphology to optimise light harvesting in different environmental conditions.

Buoyancy Control

Many species of diatoms are planktonic. To sustain photosynthesis, diatoms must remain suspended in the aquatic environment (Hamm, 2005). Conventionally, diatoms were thought to be inert, except for certain benthic species capable of gliding. However, studies have demonstrated that diatoms possess mechanisms to modulate their buoyancy, enabling them to maintain their position in the water column or adapt their buoyancy as a response to environmental factors such as light and nutrient availability (Falciatore et al. 2000; Falciatore & Bowler, 2002). Diatoms can regulate their buoyancy by manipulating their density, which is achieved through a range of physiological processes such as bio-silicification, carbohydrate ballast, and ion replacement within their vacuoles (Arrieta et al., 2020).

Diatom frustules are multifunctional structures that serves many vital roles. As previously stated, diatoms face various mechanical obstacles that affect their survival. In particular, pelagic diatoms must successfully overcome the challenge of simultaneously being lightweight and mechanically resilient. This combination makes them highly interesting for technological applications, such as in the fields of lightweight engineering and architecture (Kooistra & Pohl, 2015), where engineers and scientists seek solutions to minimize weight while maintaining mechanical performance.

1.4 Technological background

1.4.1 Mechanical background

In assessing mechanical performance, it is imperative to consider several factors. In many cases, a critical factor is stiffness (Baumgart, 2000). that depends on the type or load that is applied. In this study, the focus will be set on bending stiffness (K_B). This quantifiable measure refers to the ability of a material or structure to resist deformation or bending when subjected to a load or an applied force (Gross et al., 2006). According to Hooke's law stiffness can be defined as the ratio of applied force F to the resulting displacement δ_{max} and depends on the material and the structures shape and dimension.

$$K_B = \frac{F}{\delta_{max}} \tag{1}$$

Another measure directly related to stiffness is the second moment of area I which is a geometrical property used to calculate the deflection of a beam caused by a moment or force applied to the beam (Gross et al., 2006). I depends on the geometry of the cross-section, where the distance to the neutral axis plays a crucial role. Bending stiffness is influenced by Young's modulus E multiplied with I, leading to the following relationship:

$$K_B = E \times I \tag{2}$$

Yet another pivotal factor in the context of mechanical performance is stress. Stress is generally quantified as force per unit area and represents the internal stress of a structure or material when subjected to an external load (Shigley et al., 1985). For linearly elastic materials and small deformations, stress is proportional to displacement. Assessing the stress distribution in a structure is important to assess the load-bearing capacity and to prevent localized failure due to stress hotspots. In this context, the axiom of uniform stress emerged, which is a simplified concept stating that an elastic material subjected to an external load should have a uniform distribution of stress (Mattheck & Mattheck, 1998). Thus, an even stress distribution in a structure makes it more resilient towards failure, while stress concentrations make it more vulnerable. To analyse the stress distribution in a structure, von Mises stress is an important tool (Shigley et al., 1985). Von Mises stress σ_{VM} is a comprehensive measure, that considers the combination of normal and shear stresses and is commonly used in simulations to assess mechanical performance.

1.4.2 Simulation and parametric design

Computer-aided engineering (CAE) and computer-aided design (CAD) are complementary methodologies (Raphael & Smith, 2003). CAD involves the computer-aided creation and modification of designs, while CAE involves the simulation and analysis of those designs. Parametric design is a subcategory of CAD and is a design method in which the parameters or variables that define the shape, size, and behaviour of a model are specified mathematically or algorithmically (Monedero, 2000). These characteristics may be modified and altered, while relationships are maintained, to investigate various design possibilities and setups, with changes transmitted automatically throughout the model. Once the workflow is set up, the use and adaptation do not require deep knowledge of parametric design (Harding & Shepherd, 2017).

Many software enables parametric design by using low code. Low code is an approach that uses visual programming interfaces to simplify and accelerate the process of programming (Coenders, 2021). In parametric design, this is realised by providing pre-built components that allow to build and deploy parametric workflows without the need for coding language. By connecting the inputs and outputs of different components a workflow can be created which is similar to a script in traditional programming. Figure 1.3 shows an example of a simple workflow used to construct a vertical row of four spheres. First, a point is constructed, which serves as the central point of the sphere, by connecting its output to the input of the sphere component. A number is input to define the radius of the sphere. Then the component “Linear clones” is used to clone the input geometry. The cloning is controlled by a row of parameters, such as the directions and counts of clones. Parameters such as the size of a sphere can be easily adjusted afterwards, and the solution is automatically recomputed.

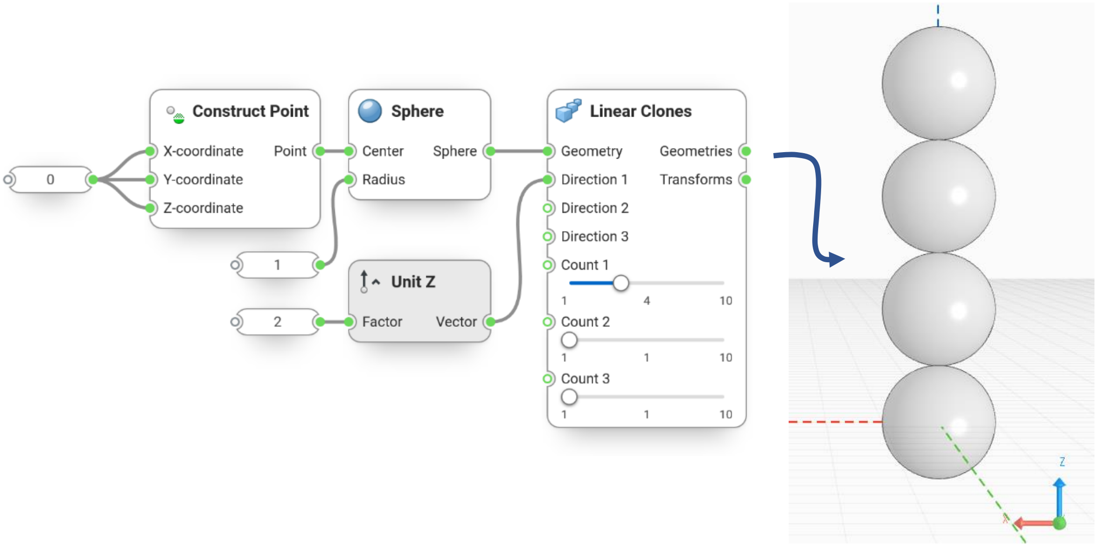

Figure 1.3. Parametric design in the form of low code to model a row of spheres created with the software Synera.

Simulation can then be used to analyse the behaviour of the created design. It involves creating a virtual environment that can accurately mimic the behaviour of a real-world system or process (Coenders, 2021). A possible use for simulation is to model the mechanical performance under bearing. A common computer-based simulation approach is finite element analysis (FEA) which is used to numerically solve physical and technical problems based on the finite element method (FEM) (Hartmann & Katz, 2004). These problems can be described by differential equations, which are often too complex and time-consuming for analytical calculation. FEM allows for realistic solutions to corresponding calculation tasks and is therefore widely used in structural mechanics. The general principle of this approach is to break down a complex geometry into smaller, simpler sections called finite elements which are connected by nodes. The relationships between these elements can be represented by a system of equations and solved numerically. The totality of the elements that comprise the model is defined as a mesh (Gokhale, 2008). The analysis considers different criteria that need to be defined in the simulation setup. These include material properties, boundary conditions, and mechanical loads in the form of external applied forces and constraints to predict the performance of the structure. The mesh of an FE model is a crucial factor for the accuracy of numerical results in a simulation. The finer the mesh, the more precise and consistent the results (Pegg et al., 2013).

There are various types of elements available for representing a finite element model, and their usage depends on various factors such as the complexity of the geometry, the physics being simulated, and the available time (Lee, 2012). The main difference between these elements is their dimensions. The most important element groups are one-dimensional (1D), two-dimensional (2D) and three-dimensional (3D) elements. For example, 2D elements, also called shell elements, are suitable for geometries, in which one dimension is significantly smaller than the other two, as in plate-like structures.

The generated mesh also forms the basis for implementing shape optimisation procedures, which are commonly used in mechanical engineering. Among these algorithmic optimisations are topology optimisation and dimensioning optimisation, which includes thickness optimisation (Christensen & Klarbring, 2008). Topology optimisation involves investigating the optimal distribution of materials within a given design space, under consideration of specified conditions (Bendsoe & Sigmund, 2003).

For this study, the topology optimisation employed is based on the SIMP approach, which stands for “Solid Isotropic Material with Penalization” (Rozvany et al., 1992). The optimisation algorithm seeks to find the optimal distribution of material that minimizes a predefined objective function, such as minimizing compliance (maximizing stiffness). This is achieved by systematically varying the design variable to achieve a homogenous distribution of stress (Bendsoe & Sigmund, 2003). This variable, referred to as the normalised density ρ_n, is defined as the ratio between the element density ρ_i and the initial element density ρ_i^0. It is directly related to Young’s modulus, the ratio of stress to strain.

$$\rho_n = \frac{\rho_i}{\rho_i^0} \tag{3}$$

$$\text{with } 0 < \rho_n < 1$$

Elements with low density of $\rho_n = 0$, represent a void region with a diminished modulus of elasticity, while elements with high density of around $\rho_n = 1$ indicate fully solid regions with the maximum modulus of elasticity (Christensen & Klarbring, 2008). The resulting density distribution gives valuable insights into the paths of load transmission in an object.

Unlike topology optimisation, which involves the redistribution of material, dimensioning optimisation focuses on refining the existing structure by optimising numerical values (Christensen & Klarbring, 2008). In the scope of thickness optimisation, this includes parameters such as the thickness of a plate. To carry out this optimisation, the elements are initially assigned a uniform thickness. Subsequently, during the optimisation process, the assigned value is iteratively adjusted for each element within a predefined interval and number of iterations. The purpose of thickness optimisation is to find the most efficient thickness distribution that meets the specified design criteria and performance objectives. This can involve minimizing displacement while satisfying specified constraints such as a maximum mass. As a result, each element obtains its own unique set of optimised dimensions.

1.5 Diatoms from a biomimetic perspective

1.5.1 The field of biomimetics

Through millions of years of natural selection, evolutionary mechanisms have led to organisms that are highly adapted to their environments (Darwin, 1859). The result is a high diversity of life forms, each with its own unique set of features optimised to improve their chances of survival and reproduction. The constant development of technologies and scientific methods enables the observation and understanding of the way living organisms have evolved to adapt and thrive in their respective environments (Nachtigall & Pohl, 2015). An increasingly well-founded understanding of the natural world enables scientists and engineers to learn from nature. Based on this idea, a continually growing scientific discipline known as “biomimetics” has emerged.

Biomimetics is defined by Nachtigall (2003) as “the transfer of principles and systems from living organisms to technology”. This does not imply the mere mimicking of nature, but rather comprehending the fundamental principles of natural systems and includes the three steps of research, abstraction and implementation (Nachtigall, 2010). The fundamental idea of biomimetics is that natural organisms have already solved many of the challenges we face. By studying those solutions, scientists and engineers can gain insight into addressing analogous technological questions and develop more efficient, sustainable, and adaptive technologies (Nachtigall & Pohl, 2015). Biomimetics is significant in the realm of science, as it can bridge biology-oriented and technology-oriented disciplines (Nachtigall & Pohl, 2015). It adopts a holistic approach, embracing complexity and interdependence.

1.5.2 State of the art

The attributes and functions of the diatom frustule that were previously discussed have captured the attention of scientists in the field of biomimetics. Especially their frustules' unique material, optical properties and intricate structures inspired applications in various industries such as nanotechnology (e.g., Losic et al., 2006), architecture (e.g., Kooistra & Pohl, 2015), photonics (e.g., Jantschke et al., 2014) and materials science (e.g., Gebeshuber et al., 2002 & 2003). The focus of this study shall be set on the structural aspects of the frustule and their potential in lightweight engineering, thus, applications in other areas will not be discussed further.

Mechanical properties are difficult to study in plankton, as in situ observations are challenging (Hamm & Smetacek, 2007). Although mechanical properties of diatoms have recently been studied more thoroughly (e.g., Cvjetinovic et al., 2023; Aitken et al., 2016), experimental tests, such as nano indentation often bring inaccuracies and are destructive. Therefore, computer-aided approaches, such as the combination of parametric design and simulation can be a useful tool to complement theoretical and experimental approaches to better understand functional morphology and biomimetic solutions inspired by diatoms. Studies of this interdisciplinary approach have been successfully applied in the last decades to determine the mechanical properties of diatom frustules (e.g., Hamm et al., 2003; Topal et al., 2020; Lu et al., 2015).

Hamm et al. (2003) analysed the strength of several centric and pennate diatoms, revealing that the frustules were able to withstand forces equivalent to a maximum of 700 t/m^2. Additionally, they were able to use simulations to show that removing the ornamented structures and adding a simple thickening of the frustule with the same amount of material led to more than 70 % higher von Mises stress and displacement values compared to the unaltered ribbed frustule models. Zglobicka and Kurzydlowski (2022) used different microscopy methods to create simulations of a computer-based model of parts of the frustule under bearing. They concluded that the ribbing structures significantly improve the resistance against localized forces. It was also proven in several studies, that the architecture of the frustule leads to a heterogenous stress distribution when force is applied (Aitken et al., 2016; Hamm et al., 2003). Costae (Ribs) smoothly deflected stress peaks by absorbing stress from more vulnerable areas such as the Areolae. Gutiérrez et al. (2018) performed simulations to analyse the unit cell of *Coscinodiscus* sp. with varying dimensions of their geometrical features. Three-point bending simulations reveal that the honeycomb sandwich structure constitutes to the high strength observed in *Coscinodiscus* sp. This is an important structural attribute, as local stress hotspots in a structure increase the risk of failure.

Studies have been conducted to create diatom-inspired lightweight structures, such as Maier et al. (2013), who employed a method to use a suitable natural archetype, such as radiolarians, for a corresponding technical challenge, as a design space to create lightweight design solutions. Other studies were conducted in architecture to create adaptive models. Fattahi et al. (2013) used a biomimetic approach to create a diatom-inspired hierarchical envelope system in façade design. The porosity of the envelopes could be altered by an adaptive pattern that responds to measurements of daylight and airflow. Breish et al. (2023) presented two novel diatom-inspired approaches to optimise the stiffness of plates and cellular solids. Inspired by *Auliscus intermidius* and *Triceratium* sp. a gradient material distribution strategy was employed. The authors were able to produce models with maximum displacement values close to the SIMP-based topology optimisation, even outperforming it in some cases. An overview of further applications of diatom-inspired lightweight engineering is given by Kooistra and Pohl (2015).

Even though recently more biomimetic approaches for diatom-inspired structures emerged, there have been no studies on developing stress-adaptive diatom-inspired stiffening structures with automatic workflows such as parametric design.

1.6 Study objectives

The study aims to explore the potential of diatom frustules as an inspiration for adaptive surface stiffeners for industrial purposes. It is assumed that diatom-inspired lightweight structures can offer more efficient surface-stiffening than conventional engineering methods. An interdisciplinary approach was applied, combining methods from the fields of biomimetics, biology and engineering. The primary objective of the thesis was to implement and compare different approaches to create diatom-inspired stress-adaptive surface stiffeners and to examine their potential in comparison to conventional methods.

By exploring the potential of diatom-inspired stiffening structures, the study seeks to contribute to the development of sustainable and efficient engineering solutions. The interdisciplinary nature of biomimetics lays the foundation for progress in science, by combining knowledge and methods of different fields. This allows researchers to address scientific questions from a different perspective. Thus, it gives a framework for innovation, enabling the development of new methods of investigation, and the application of the principles of biomimetics to create novel scientific methods.

2 Materials and Methods

2.1 Experimental approach

The objectives were explored by following the approach depicted in Figure 2.1. To pursue the aim of the thesis, two main approaches were used to minimize the displacement of a plate. The biomimetic approach comprised several steps. Firstly, a biological analogy was identified for the given technical problem, which in this study was represented by diatom frustules. Frustules of different genera were then analysed using various microscopic techniques to examine their morphological characteristics. These geometric features were then abstracted and applied to a reference model with computer-aided methods. The reference model consisted of a computational model of a plate, with defined load cases and boundary conditions. The abstracted principles were computationally analysed and combined to create various stress-adaptive models. Several bio-inspired approaches were explored, including a rib approach, a comb approach, and a combined approach that utilized stress-adaptive sandwich structures. Furthermore, algorithmic optimisation was applied to the reference model to compare the bio-inspired models with a conventional approach in mechanical engineering. The resulting models were evaluated and examined based on simulating their mechanical performance, specifically in terms of their maximum overall displacement. Subsequently, the framework conditions were varied to investigate the robustness of the established methodology. Thus, the potential of this approach could be evaluated regarding computational effort, mechanical performance, and its limitations.

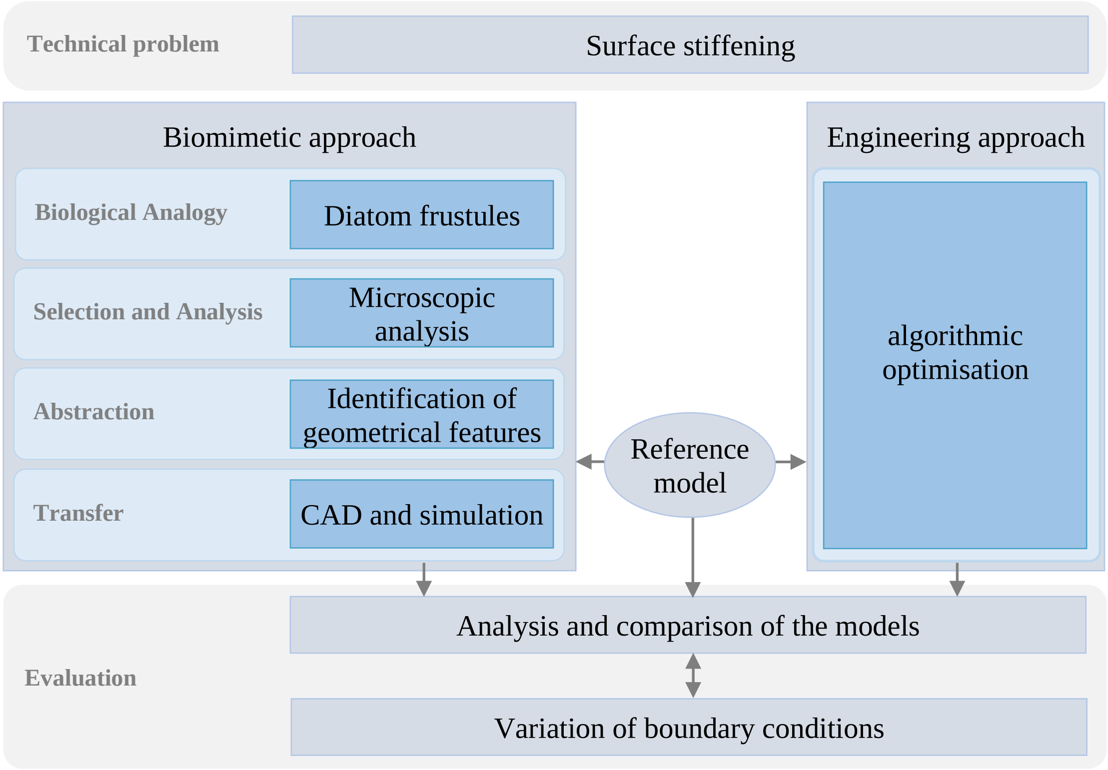

Figure 2.1. Overview of the approach undertaken in the present study.

2.2 Characterisation of diatom frustules

2.2.1 Microscopic analysis

Sample Preparation

The samples for the analysis were provided by the Alfred Wegener Institute (AWI) and originated from their collection of diatom cultures. Some cultures contained only one species which was isolated from a sample and propagated. Other cultures contained a mix of genera. The study area was not provided. The diatom samples were stained using the in-vivo stain Lysosensor DND-160 (PDMPO, Life Technologies) according to the protocol by Desclés et al. (2008). The diatoms were grown in an f/2 medium (Ryther and Guillard, 1962), dosed with Lysosensor DND-160 at a final concentration of 125 µM. For the freshwater diatoms, the WC medium by UTEX was used.

To remove the organic contents of the cells and the frustulin membrane coating the frustule, the diatoms were washed in deionized water four times by centrifuging at 453 g and subsequent removal of the supernatant. The pellet was then dosed with a saturated KMnO4 solution and incubated for 24 hours at ambient temperature. This solution was carefully mixed with an equal volume of concentrated HCl and boiled until the mixture cleared. To remove the chemicals, five washing steps followed as described above.

The cleaned frustules dried on microscopic slides mounted in Prolong Antifade Glass mountant (Thermo Fisher). For SEM, the cleaned frustules air-dried on a round 10 mm cover slide and mounted on SEM stubs using double-sided conducting carbon tabs. To ensure good conductivity, the samples were sputter-coated with a 20 nm gold/palladium layer. The samples for light microscopy were cleaned and mounted in Naphrax (Biologie-Bedarf Thorns), a synthetic resin for diatom analysis with a very low refractive index of 1.71.

Image generation

The diatom frustules were analysed with three microscopic methods: Light microscopy (LM), Scanning Electron Microscopy (SEM) and Confocal Laser Scanning Microscopy (CLSM).

Light microscopy: Images were taken with a Zeiss Primo Star iLED which features an integrated digital camera. Images were taken with a Zeiss Plan Apochromat Lens with a magnification 40 and numerical aperture of 0.65 and the software Zeiss Labscope.

Scanning Electron Microscopy: The SEM images were captured with an FEI Quanta 200 FEG SEM (FEI, Hillsboro, OR, U.S.A). The SEM was set to 10 kV accelerating voltage, and the images were captured with secondary electron imaging (SEI).

Confocal Laser Scanning Microscopy: The CLSM images were obtained using an Olympus Fluoview FV10i confocal laser scanning microscope with an excitation wavelength of 405 nm and emission wavelength of 540 nm. To match the fluorescent growing medium's excitation. The images were acquired using a 60x oil immersion objective with a numerical aperture of 1.4. In one focal plane, the sample was scanned in a raster. A z-stack was formed by successive slices, which were then processed to generate a 3D image.

Post-Editing

The images obtained with the CLSM were further processed with Huygens Essential (version 22.10) to increase the solution and quality to then be analysed with the software Imaris to transform the images into 3D models.

2.2.2 Characterisation of structural features

The last step of the microscopic analysis was the examination of the images. For the unidentified diatoms, taxonomic keys were used to identify genera based on characteristic features of the frustule. The morphological features within the different genera do not differ significantly and identification at the species level is not necessary for the purpose of this study. The structural elements were then evaluated in terms of their properties and their significance for mechanical performance. By understanding the purpose of the frustule’s structural characteristics, knowledge of the form and function of the frustules was gained to abstract and transfer their principles. The focus of this study lies on the structural properties, therefore the material properties of the frustules were neglected.

2.3 Development of surface stiffening structures

2.3.1 Reference model

Mesh study

The mesh of an FE model cannot be arbitrarily fine due to constraints regarding numerical and time effort. Thus, a mesh study was carried out to achieve a sufficient element density for the model. The mesh of a model is considered sufficient if the value of the target variable, for this study δ_{max}, differs by less than 5 % in three consecutive discretization steps (Pegg et al., 2013).

The mesh study was performed on a model with a stiffening structure, exhibiting a hexagonal pattern with comb size $c_s = 11\ mm$ according to the model described in the following sub-chapter. This model was chosen, as the reference model does not have any complex geometries and to assure an adequate meshing for the models. The model was gradually refined from an average element size $l_e = 6\ mm$ 5 to $l_e = 1\ mm$, with 1 mm steps from 6 to 3 mm and 0.5 mm steps from 3 to 1 mm. The thickness of the elements was not affected by this study and was assigned in the ongoing process.

Set-up of the reference model

In this study, parametric computer-aided design was employed to develop different models and FEA was performed to analyse their mechanical performance under different conditions.

For the development of the models, the low-code-based software Synera (version 23.05) was utilized. The mechanical behaviour of each constructed model was simulated with the software Altair Optistruct (version 2019.2) which is implemented in the Synera interface and was integrated in the parametric workflow. The meshing was performed with the Optistruct mesher, implemented in the Synera software. All models were meshed with shell elements consisting of rectangular (QUAD4) and triangular elements (TRIA3) (Lee, 2012).

To be able to compare different stiffening structures, a reference model was set up as a simple plate. This model consisted of a planar rectangle with the dimensions shown in

Figure 2.2. The model was constrained with fixed support along the red lines, which means that the movement was restricted in all degrees of freedom (three translational and three rotational). A static out-of-plane load (F) was applied onto the plate (blue semi-circle) with a radius of 5 mm in the positive z-direction, with a magnitude of 1 kN. In the next step, a mesh was generated for the model with the mesh size defined according to the results of the previous mesh study. The thickness t of the plate was set to $t = 2.78\ mm$ to result in a total mass m_t of 1 kg. Structural steel is assigned as the material, with the properties specified in Table 2.1.

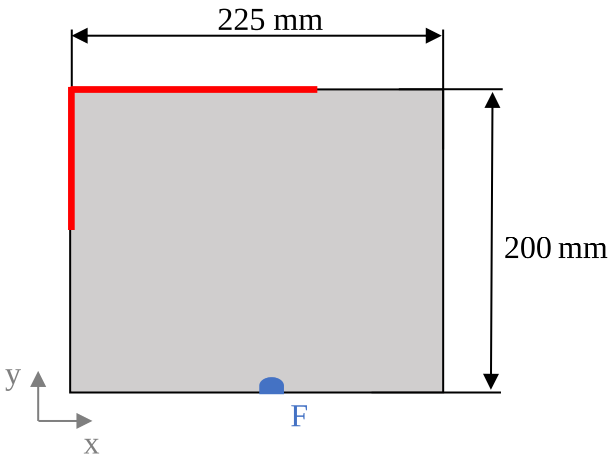

Figure 2.2. Sketch of the reference model with its dimensions. The red line indicates the fixed support, and the blue semi-circle depicts the area where F was applied in z-direction.

Table 2.1. Material properties of Structural Steel, which was used for the simulation of all models. The properties were given by the AWI.

	Structural Steel
Density [kg m^{-3}]	8000
Young’s modulus [MPa]	193 000
Poisson ratio [-]	0.28
Maximum yield stress [MPa]	360

Afterwards, the reference model was numerically solved to analyse its stiffness. As the models were subjected to the same load case and had the same material properties, the relative stiffness could be analysed solely by comparing the maximum displacement δ_{max} of the models. The von Mises stress σ_{VM} distribution in the reference model resulting from this load case served as the basis for the models that followed.

2.3.2 Engineering approach: Thickness optimisation

To analyse and compare the performance of the bio-inspired approaches accordingly, thickness optimisation was applied to the reference model to represent a conventional engineering approach. For the optimisation, the “Optistruct Optimizer” implemented in Synera was used. The 2D elements were initially assigned a uniform thickness according to the reference model. The possible element thickness was constrained to be between 1 mm and 15 mm. A design constraint was set to match a total mass of 1 kg. The optimisation objective of the algorithm was defined as minimizing δ_{max}. The maximum number of iterations was set as 80. The optimised model typically results in an uneven surface which should ideally be remodelled into a smooth 3D mesh. As the other models were constructed with 2D meshes, this model was also not further converted, to maintain comparability.

2.3.3 Rib approach

The first optimised model consisted of a combination of geometrical features, such as combs, ribs and sandwich structures. In this chapter, a combination of design methods was used with different software, including the steps of topology optimisation, manual reconstruction, and parametric design, making it an exception from the following models.

Topology optimisation

Initially, a topology optimisation was performed, considering load case 1 and the previously described setup of the reference model. To create the optimised structure, an area was then specified, which was defined as the remaining area A_r of the original area A of the reference model. Additionally, a restriction was imposed on the dimension of individual pathways to ensure the formation of clear and distinguishable structures. The objective of the algorithm was defined as minimizing weighted compliance, which means maximizing stiffness. The minimum dimension was set to 3 mm and the maximum dimension was set to 9 mm. Three optimisations with $A_r = 15\ \%, 20\ \%\ and\ 30\ \%$ were carried out for the reference model to highlight the paths of load transmission as effectively as possible. To facilitate result evaluation, the optimised models were visualized using HyperView. Furthermore, the optimised model which depicted the load paths most effectively was exported as a surface in a STEP format and imported into the CAD-software Rhinoceros 3D (version 6 SR9) for the subsequent process.

Manual reconstruction

The previously imported surface of the optimised model served as a template for the placement of continuous ribs to stiffen the surface. The ribs were created in Rhinoceros 3D by manually placing curves which followed the paths of the template surface, which could then be extruded in Synera. Additionally, a surface was designed by offsetting the curves by 1.5 mm in both directions on the plane, resulting in T-shaped ribs formed atop the existing ribs.

Parametric design

The curves and the surface were imported into Synera, enabling the parametric addition of smaller comb-like ribs that interconnected the continuous ribs. These combs were created by initially placing points on the curves, maintaining a 5 mm distance between each other. The resulting points were used as input points for a Voronoi diagram generating comb-like connecting ribs. A more detailed description of the construction of combs will be given in the following chapter. The connecting ribs were extruded with a rib height h_c of $5\ mm$ in the positive z-direction. The continuous ribs were extruded in the same direction with h_c adjusted to result in a total mass of 1 kg.

2.3.4 Comb approach

In this chapter, an alternative approach was followed. The abstracted comb features of the diatom frustules were transferred to the plate and were analysed stepwise, including the comb size, uniformity, adaptive patterns and sandwich structures. For comparability between the models, m_t was set to 1 kg with a uniform thickness for the plate of $t = 1\ mm$ and $t = 1.2\ mm$ for any additional stiffening structures. All following patterns were created as curves, which were then extruded in the positive z-direction to create a ribbing structure. The height of the ribbing structures was uniform and calculated to match the restriction of $m_t = 1\ kg$. The resulting models were analysed regarding their maximum displacement under the application of the previously defined load case.

The basis for the different comb patterns in this study was a Voronoi diagram, which is a mathematical method used to divide a space into regions based on proximity to specified points (Aurenhammer, 1991). In a two-dimensional space, it is generated by computing the perpendicular bisectors of the line segments between each pair of points and intersecting these bisectors to form the edges of the Voronoi polygons. First, a 2D point distribution is generated on the surface, which will control the shape and distribution of the combs (Figure 2.3)

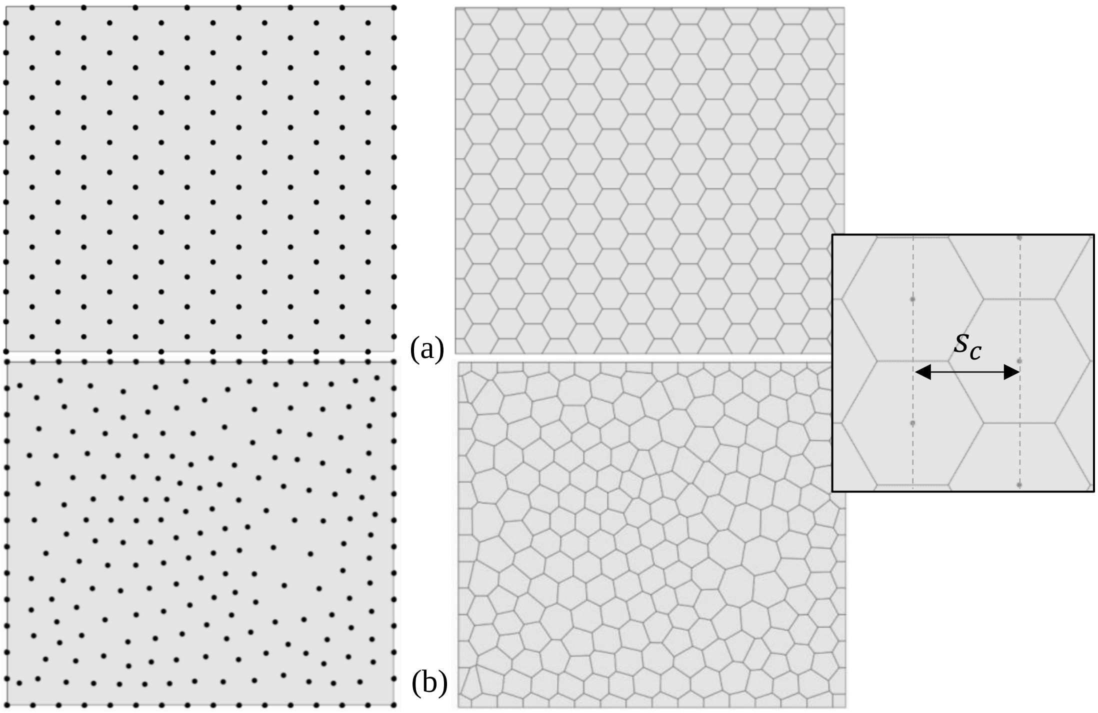

Figure 2.3. Voronoi combs, based on (a) left: a point grid based on mathematical relationships, right: resulting uniform hexagon pattern after application of the Voronoi diagram and a definition of the comb size s_c. And (b) a randomised 2D point distribution, right: resulting irregular polygon field after application of the Voronoi diagram.

Comb size

A first study was conducted to analyse the influence of the comb size (s_c) and rib height on δ_{max} for a model with regular hexagonal combs. A regular point field was created manually to result in uniform hexagons, based on a mathematical distribution considering that all interior angles of a hexagon are 120 degrees each (Figure 2.3, a). To analyse the size, s_c was gradually increased from 5 mm to 25 mm in 2 mm steps. The comb size is here meant as the distance in the x-direction of the centre points of two rows of hexagons, as indicated in Figure 2.3.

Uniformity

Subsequently, comb patterns with different degrees of uniformity were studied. In this part of the process, two different point distributions were used to apply a Voronoi diagram to compare a model with regular hexagons and a model with irregular polygons. The regular model was chosen from the previously performed size study, with a favourable s_c based on the maximum overall displacement. For the second model, a random point distribution was created, to generate an irregular pattern of different polygons (Figure 2.3, b). The feature "point distribution" in Synera creates a randomised point distribution, which is controlled by defining a global distance value d_c, which defines the average distance between points. This value was set based on the value s_c for the regular pattern.

Stress-adaptive patterns

For this approach, the comb patterns were constructed in a way that they adjusted to the von Mises stress distribution caused by load case 1. In the previous sub-chapter, combs with roughly uniform sizes were used to create the patterns. However, for this sub-chapter, the density of the combs was varied based on the stress distribution in the plate. This means that areas with higher stress values had a higher density of combs, resulting in smaller comb sizes, while areas with lower stress values had a lower density of combs. For this, the calculated stress distribution of the reference model was used, which needed to be translated into a stress field (SF). To achieve that, the centres of the finite elements and the stress response in said points were extracted. The field then consisted of points with individual stress values, the SF was further used to manipulate the comb patterns. The thickness of the elements, the height of the ribs and the mass of the model were constrained in the same way as in the previous models.

Three different patterns were aimed for. The first one, pattern A, consisted of irregular polygons with varying densities. Similar to Figure 2.3 (b) a random point distribution was used, but instead of one global distance value d_c to control the point distribution, in this workflow the previously defined stress field was used to manipulate the density locally. Subsequently, the stress values of the field were normalised and then remapped to values between 8 and 30, which served as local distance factors. Afterwards, the Voronoi combs were applied.

Patterns B and C were created according to the approach illustrated in Figure 2.3 (a). For both, the feature "transform morph" was used, which distorts a geometry based on a spatial field of local scaling factors. As a first step, the values of the SF were normalised and remapped to values between 0 and 3. Afterwards, the values were additionally evaluated as x for the mathematic expression as follows:

$$F(x) = 1/(1+\exp(-((x-0.7)*10))) \qquad (4)$$

By applying this expression, the values were changed from a linear distribution to an S-shaped distribution with midpoint $P_m = (0.5, 0.7)$. This means that the values above 0.7 were increased towards 1 and the values below 0.7 were decreased. Thus, the values were mapped between 0 and 1, with higher contrast between the low and high values. The resulting values served as the scaling factors s_f from 0 to 1. So that the maximum stress value equals $s_f = 0$ and the minimum stress values equal $s_f = 1$, which means no distortion. These values were then set as local fields and combined into one field. This process overlays the local fields, thus the scaling factors of 0 are not infinitely small but morph the pattern smaller. The resulting field of scaling factors thus distorted the hexagon pattern. For pattern C, the same method was applied, but instead of distorting the curves of the hexagon field, the centre points were morphed and the Voronoi field was applied after the distortion.

Sandwich structures

A new feature was introduced for this sub-chapter, defined as sandwich structure, which was added on top of the combs, to generate a structure that shall resemble the foramen found in many diatom genera. The sandwich structure was generated for the model with the lowest δ_{max} chosen in the previous section. Figure 2.4 shows the steps to create this structure for a simplified example of a single hexagonal comb, which was created for the whole model. For this study, different offset distances (d_o) from 0.5 mm to 1.5 mm were applied and the maximum overall displacement and rib height were compared.

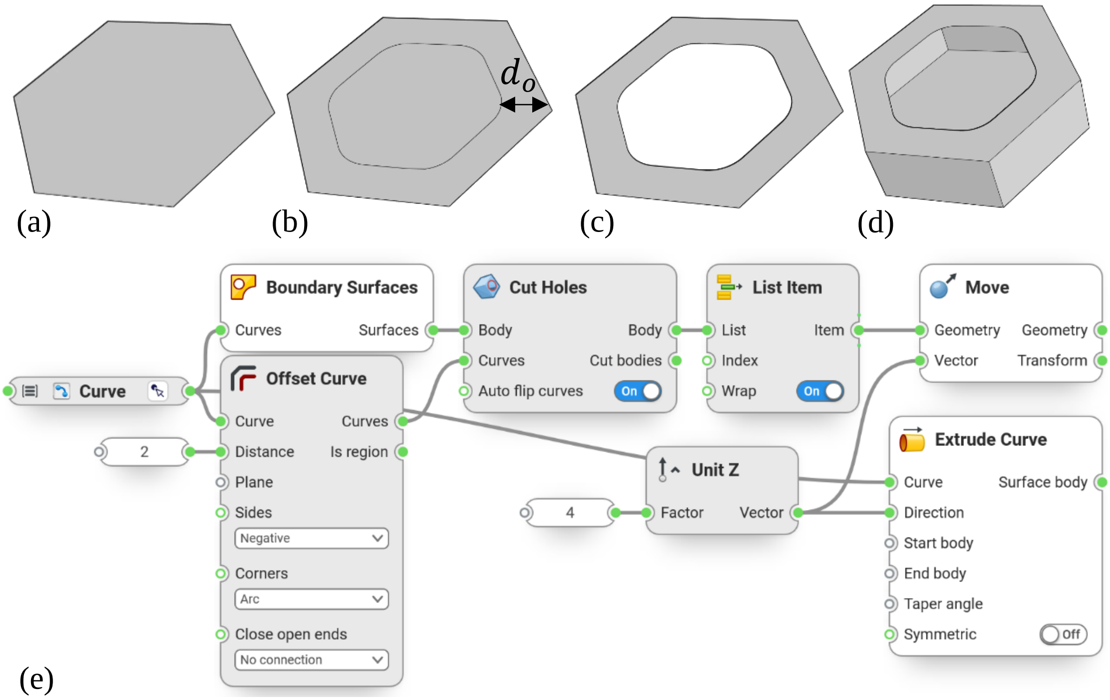

Figure 2.4. Simplified process of creating a hexagonal comb with a sandwich structure. (a) Surface-based on a boundary curve, (b) offset of the boundary curve with offset distance d_o, (c) resulting surface after cutting out the inner surface, (d) move that surface up, extrude the boundary curve and combine with the boundary surface and (e) the associated workflow in Synera. The outputs of the white features are the ones that make up the final geometry.

2.3.5 Combined approach: Stress-adaptive sandwich structures

The findings obtained from the individual steps conducted in the preceding chapter were integrated synergistically to create a novel model. This chapter included the creation of two models both based on the pattern with the lowest maximum displacement obtained from the sub-chapter on uniformity. In contrast to previous models, a variable rib height was employed. This rib height was tailored to match the stress field of the reference model and ranges between 0 and 15 mm. Furthermore, a sandwich structure was introduced but selectively applied only to regions exhibiting high stress values σ_{VM}. The stress field of the reference model was divided into distinct regions according to the percentages outlined in Table 2.2. These intervals were chosen intuitively, as the resulting geometry effectively portrays the different areas by representing the division of the stress field.

Table 2.2. Stress intervals in the percentage of the maximum stress threshold of 600 MPa and the assigned structural features for each interval.

σ_{VM} **[%]**	**Comb height [mm]**	**Sandwich structure**
<10%	0	no
10-40%	1-15	no
40-100%	1-15	yes

No supplementary stiffening structures were incorporated in regions where stress values remained below 10 % of the maximum stress threshold of 600 MPa. Conversely, for regions with stress values exceeding 10 %, comb structures were introduced. This was achieved by initially creating a non-planar assistance surface, which enabled the adjustment of rib heights for the combs. The stress field values were translated into a comb height range spanning from 1 to 15 mm, where 0 MPa corresponded to $h_c = 1\ mm$ height and 600 MPa corresponded to $h_c = 15\ mm$.

The first step involved generating a planar point grid on the reference plate, followed by the generation of vectors to move these points. By evaluating the stress field, which was translated into heights, at each point and multiplying the apparent value with the z-unit vector, the height was assigned as the amplitude of the vector. Subsequently, the moved points served as a foundation for creating the non-planar assistance surface. This assistance surface was then used to intersect the extruded combs, resulting in a varying rib height adjusted based on the stress distribution. The addition of sandwich structures involved filtering out combs with stress values ranging from 40 % to 100 %. Only these selected combs were used to create an offset according to Figure 2.4. Other than in Figure 2.4 the offset was not cut from the base surface, but from the assistance surface by projecting the curves onto the surface. The offset distance was chosen according to the results from the sub-chapter on sandwich structures.

As a last step, a thickness optimisation was carried out as in Chapter 2.3.2. The base plate was set to 1 mm and was not part of the optimisation process, while the thickness of the combs and sandwich structures was optimised. The possible thickness was set to 0.5 to 3 mm. The objective was a minimal displacement, and a defined constraint was a maximum total mass of $m_t = 1\ kg$.

The second model was an improvement of the first model in this chapter. By analysing the results of the thickness optimisation, areas of the combs that were assigned a small thickness were reduced in area, by cutting out an oval shape. This reduction of material was used to increase the maximum rib height to 20 mm. As in the model before, a thickness optimisation was run with the same constraint and objective, but for this model, the thickness of the plate was included in the optimisation as well, with a possible thickness between 0.5 and 1.5 mm.

2.4 Variation of the boundary conditions

To analyse the robustness of the created workflow, the goal for this chapter was to explore the applicability of the combined approach for changing boundary conditions. Thus, a randomly designed non-planar surface was constructed and a new load case was defined. Two approaches were tested, a thickness optimisation on the bare surface and the improved combined model.

For the new load case, the surface was supported by a pinned support configuration, with movement restricted solely in the translatory z-direction. This restriction was applied on two opposing edges of the surface, illustrated as the yellow highlighted edges in Figure 2.5. Additionally, two static point loads were applied to circular areas on the surface, as indicated in the figure.

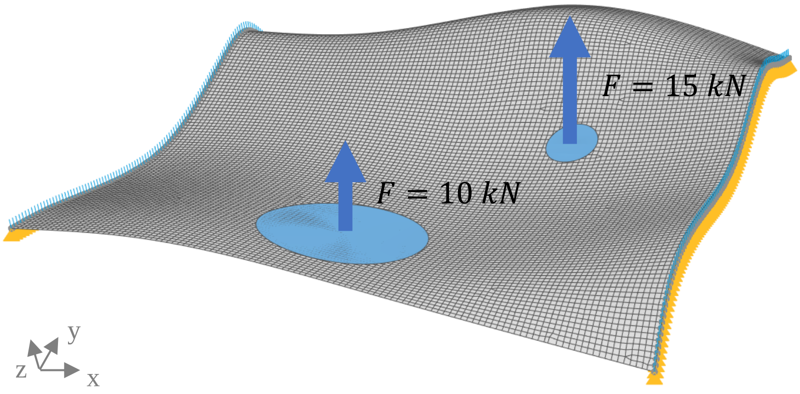

Figure 2.5. Non-planar surface and the applied configuration. The yellow triangles on the two opposing edges of the surface indicate the pinned support restricted in the translatory z-direction. The blue circles indicate the load application in the positive z-direction.

To initiate the analysis, the surface was first calculated without any surface stiffening. The thickness of the surface was adjusted to ensure $m_t = 1\,kg$. Subsequently, the resulting δ_{max} was examined. The thickness optimisation was run under the same conditions as previously defined in Chapter 2.3.2. The previously designed combined model (see Chapter 2.3.5) was built parametrically, thus, the workflow was adjusted to easily switch between planar and non-planar surfaces. The initial conditions were modified to input the new surface design and configuration. Due to the parametric nature, the automatic calculation of the stress field and the adaptive structures was enabled. The following thickness optimisation was performed as defined in the previous chapter. The subsequent step involved evaluating the surface's behaviour by analysing the maximum overall displacement of each model and verifying the suitability.

3 Results

3.1 Characterisation of diatom frustules

A total of 17 genera were identified with the microscopic methods. A full list of genera and information on their general morphology can be found in Appendix A.2. A total of about 15 images were taken with LM, about 100 images were taken with the SEM and about 40 3D images were taken with CLSM. Additional images taken with the SEM are given in Appendix A.3. The frustules exhibited a high morphological diversity, yet common geometries were observed. The analysis of all images led to two general categories to sort the geometrical features, combs and ribs, which were focused on for this study. Figure 3.1 shows an exemplary image for each microscopy method representing the two categories. As the frustules are 3-dimensional, the light microscope only allowed the imaging of one focal plane at a time. The 3D models allowed the analysis of structures from different perspectives and provided a more accurate impression of the structures. The images from the SEM provided a high degree of detail.

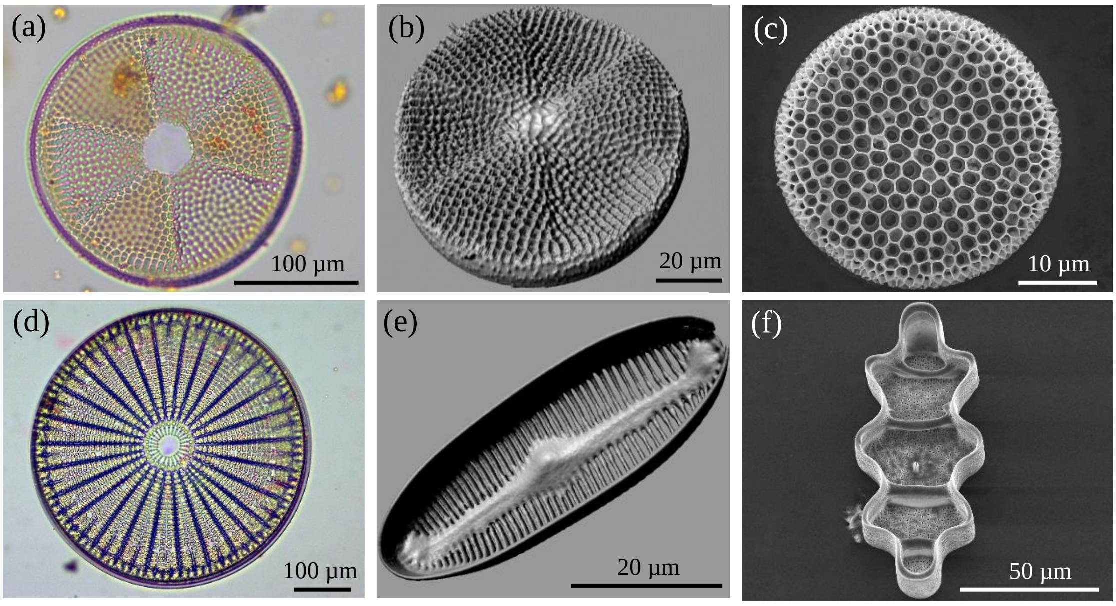

Figure 3.1. Upper row: microscopy images of diatom frustules, examples containing combs: (a) *Actinoptychus* sp. (b) *Actinoptychus* sp. (c) *Porosira* sp.; Lower row, examples containing ribs: (d) *Arachnoidiscus* sp. (e) *Pinnularia* sp. (f) *Terpsinoë* sp.; Images (a, d) were taken with LM (b, e) were taken with CSLM and (c, f) were taken with SEM.

The morphological analysis of the valves revealed that comb-like structures are mainly found in centric diatoms and strut-like structures were mostly present in the elongated pennate diatoms. The areolae that were observed in centric diatoms often displayed polygonal combs with different characteristics. In some of the analysed species, such as *Stephanidiscus* sp. and *Porosira* sp., an irregular pattern of polygons with a varying number of vertices was observed (Figure 3.2). The foramen in many centric diatoms, such as visualised in *Porosira* sp. (Figure 3.2, c) gives the areola a sandwich-like characteristic with a cross-section resembling a T-beam. In the displayed individual, part of the frustule likely dissolved as the outer porous layer was not present, such as the velum which would form the wall occluding an areola, opposing the foramen. Another recurring feature was a size gradient, specifically seen in the areolae of species with an irregular pattern such as *Porosira* sp., which exhibited smaller areolae towards the margin of the valve, decreasing in size by about 50 %. Other frustules exhibited areolae forming a regular pattern of hexagons, such as those present in *Thalassiosira* sp. (Figure 3.2, b). In most diatoms, the supporting structures were positioned on the inside of the valve, with the foramen facing to the inside, while others such as *Porosira* sp. had the foramen positioned on the outer side of the valve.

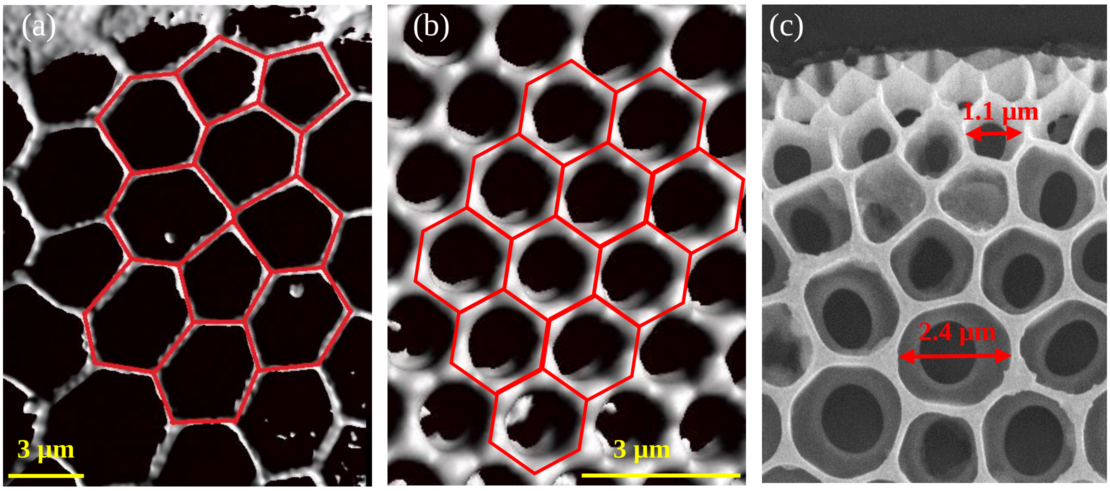

Figure 3.2. Detailed images of the Pores of (a) *Stephanodiscus* sp. (b) *Thalassiosira* sp. (c) likely *Porosira* sp., partly dissolved. (a) and (b) are images of 3D models made with the CLSM; (c) is an SEM image.

The striae showed different orientations in pennate and centric diatoms. In centric diatoms such as *Arachnoidiscus* sp. striae were radiate, while pennate diatoms had parallel uniseriate striae consisting of areolae, expanding from the sternum to the margins. Another repeatedly observed feature were costae forming ridges or struts, such as the costae radiating from the central flange of the inner valve in the genus *Arachnoidiscus* (Figure 3.3, b). Towards the free edge, these costae were thickened, resulting in a T-shaped cross-section. In pennate diatoms, these were often oriented transapically and could have a distinct axial costa along the apical axis such as *Surirella* sp. (Figure 3.3, c) or connect to the sternum such as in *Pinnularia* sp. (Figure 3.1, e). In some genera such as *Pinnularia* and *Caloneis*, the striae were alveolate and positioned within chambers. Other striking features were struts supporting the raphe canal called Fibula, such as in *Cymatopleura* sp. (Appendix, A.1).

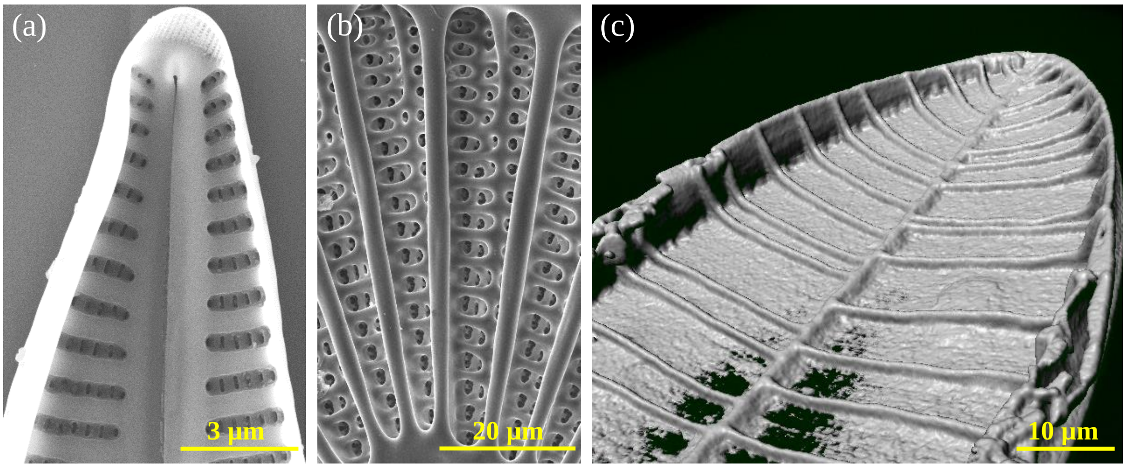

Figure 3.3. Detailed images of frustules exhibiting struts and rib-like structures found in diatoms (a) *Cymbella* sp. (b) *Arachnoidiscus* sp. (c) *Surirella* sp. (a) and (b) are SEM-images, (c) is an image of a 3D-model made with the CLSM.

The frustules exhibited hierarchical structures, often consisting of areolae which may form comb-like geometries, and costae which can form ribs and ridges. In many cases several different geometrical features were present in an individual valve, varying in their size. It is also to note that geometries observed in the frustules had no hard edges and corners, but smooth transitions and rounded corners between structures. The valves of some frustules were undulated either on the margins (e.g., *Trepsinoë* sp.) or the valve face (e.g., *Actinoptychus* sp.), resulting in crests and troughs. These features were disregarded for this study, as the shape of the reference plate was supposed to be consistent.

3.2 Development of surface stiffening structures

3.2.1 Reference model

Mesh study

The conducted study on achieving sufficient connectivity of the model with hexagonal combs led to the results presented in Figure 3.4. The graph displays the maximum overall displacement and the percentual deviation to the previous refinement step for static loading according to Load Case 1, as the mesh was refined. Throughout the conducted mesh refinement steps, the deviation of individual steps for maximum displacement fell below 5 % for an element size l_e of 2 mm and smaller. Therefore, the model was considered adequately connected for $l_e = 2\,mm$. However, since the optimised models involved more complex geometries and a uniform mesh size is preferable, the mesh size $l_e = 1\,mm$ was chosen for meshing all models.

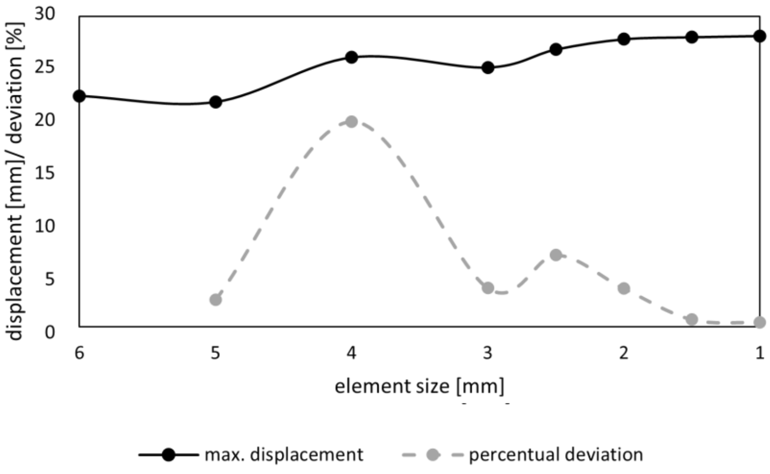

Figure 3.4. Mesh study for the hexagonal model with $c_s = 11\ mm$. Depicted are the maximum overall displacement [mm] and the deviation [%] to the previous refinement step for the average element size [mm] of the mesh.

Set-up of the reference model

The displacement plot of the reference model showed an increasing displacement towards the lower right corner, where the maximum overall displacement was assessed as $\delta_{max} = 30.85\ mm$ (Figure 3.5, a).

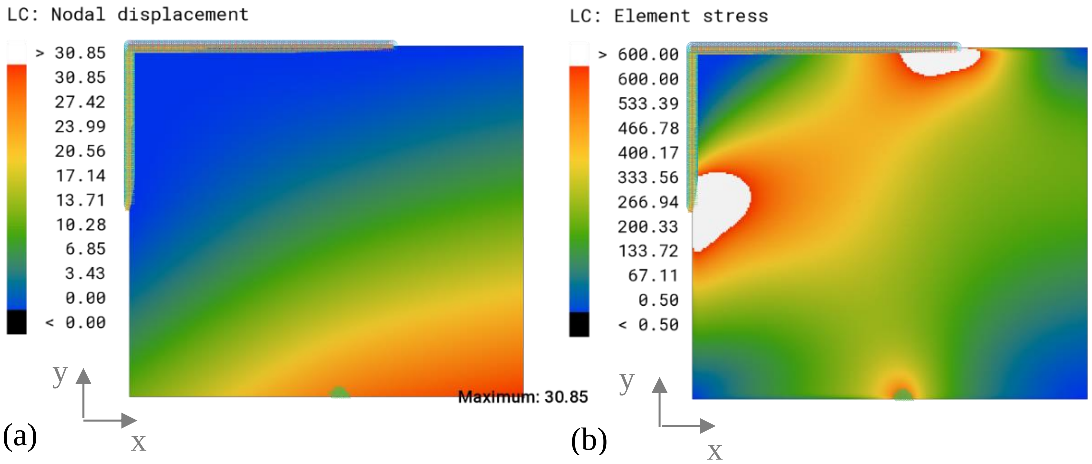

Figure 3.5. (a) Overall displacement plot and maximum overall displacement [mm] and (b) von Mises stress distribution [MPa] of the reference model under load case 1. The maximum stress threshold was set to 600 MPa.

The related von Mises stress distribution showed stress hot spots in single elements. As the stress distribution was not an objective in this study, but a reference for the patterns, the maximum threshold was changed, so that all values higher than 600 MPa, which are depicted white in Figure 3.5 (b), were changed to 600 MPa to attain a smooth stress field. Areas with higher stress were observed around the corners of the fixed support and in the area of the load application. The corners of the plate depicted stress values close to 0 MPa.

3.2.2 Engineering approach: Thickness optimisation

The thickness optimisation resulted in a discrete pattern (Figure 3.6). Most of the plate was assigned the minimal element thickness of 1 mm. Discrete rib-like areas with a maximum thickness of 15 mm and a transitioning zone with a medium thickness value formed, connecting the edges of the support to the loaded area. The maximum displacement of the optimised model was $\delta_{max} = 0.97\ mm$ (Figure 3.6, b).

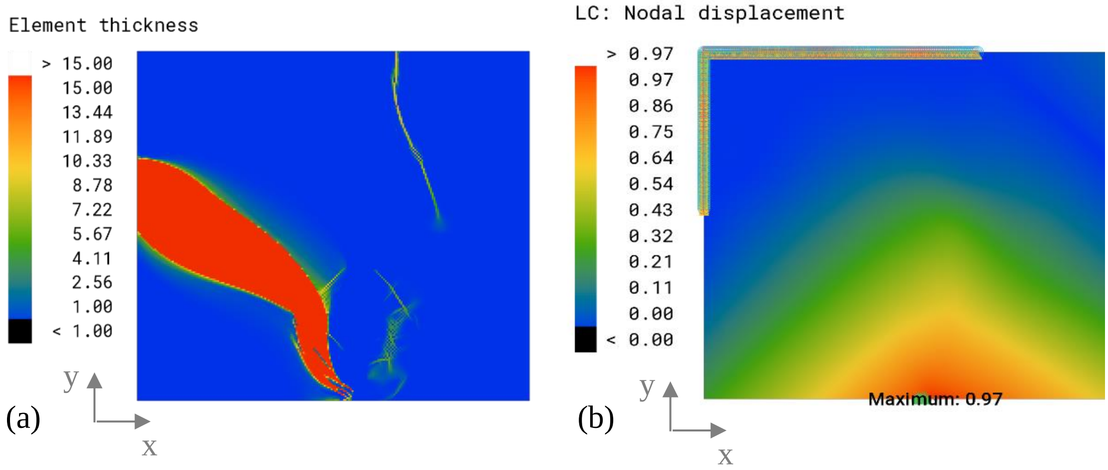

Figure 3.6. (a) Element thickness plot and (b) overall displacement plot and maximum overall displacement [mm] of the optimised model.

3.2.3 Rib approach

As a template for this model, the topology optimisation result from the calculation with $A_r = 30\ \%$ was used. The results of the other two optimisations can be found in Appendix A.4. Figure 3.7 (a) illustrates the result of the optimisation. The element density is highlighted by colour, where red areas indicate a normalised density of $\rho_n = 1$, and blue areas represent a normalised density of $\rho_n = 0$. The resulting area consisted of elongated struts with maximum density. These paths propagate from the stress peaks at the edges of the support to the area of load application. (b) shows the designed curves on the template surface. Due to the regular definition of the points, the resulting Voronoi combs had a high degree of regularity and formed rectangular comb (c). The upper surface is indicated in orange and formed the T-shape on top of the continuous ribs which had a height of $h_c = 9.36\ mm$. The maximum displacement of the model was $\delta_{max} = 6.96\ mm$ and appeared in the lower right corner (d). An additional image of the 3D structure of the model is given in Appendix A.5.

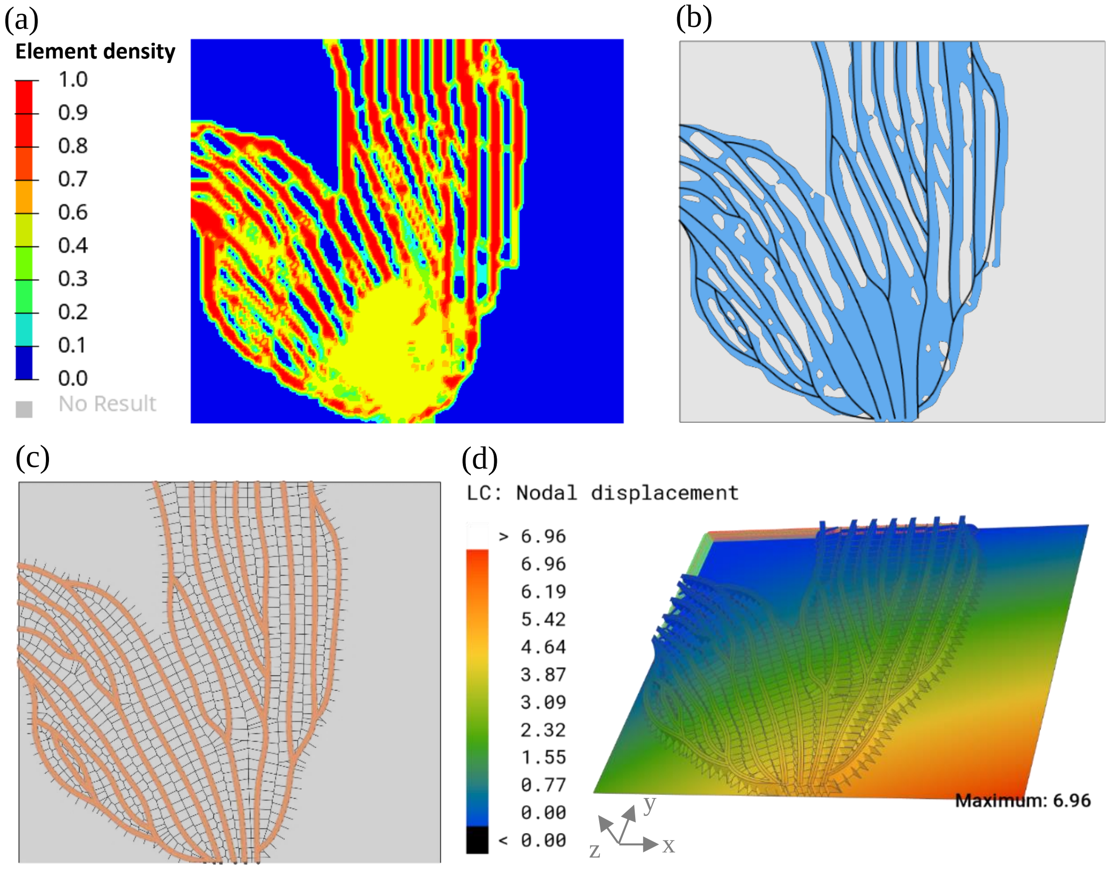

Figure 3.7. (a) Element density plot for a remaining area of 30 %, (b) extracted surface and manually recreated curves, (c) Voronoi pattern and sandwich surface and (d) the overall displacement plot and the maximum overall displacement [mm] of the rib model.

3.2.4 Comb approach

Comb size

The size study of the hexagonal comb pattern showed that c_s is directly related to the rib height, an increase in comb size resulted in a decrease of surface area and thus enabled an increased rib height (Figure 3.8). The maximum overall displacement was the highest for the smallest comb size of 5 mm and gradually decreased with an increased comb size before it started to increase slightly for comb sizes larger than 17 mm. Based on these results, a comb size of 11 was chosen for the consecutive steps, with $\delta_{max} = 20.97\ mm$. The maximum displacement was slightly lower for the comb size of 13 mm to 17 mm, but a smaller comb size was preferred, to keep the overall height of the model to a minimum.

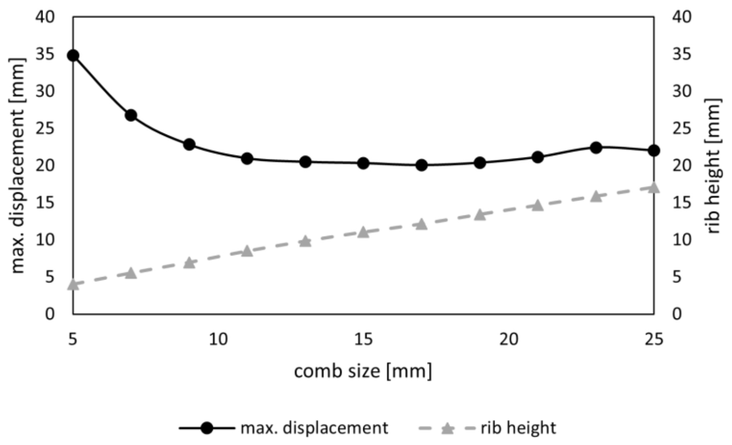

Figure 3.8. Maximum overall displacement [mm] of the model and rib height of the combs [mm], in relationship to the comb size [mm].

Uniformity

Figure 3.9 illustrates the close resemblance in maximum overall displacement between the model featuring uniform hexagons and the one with irregular polygons, with a difference of less than 0.3 mm, both occurring within the same region. The height of the combs in the hexagon model was slightly higher.

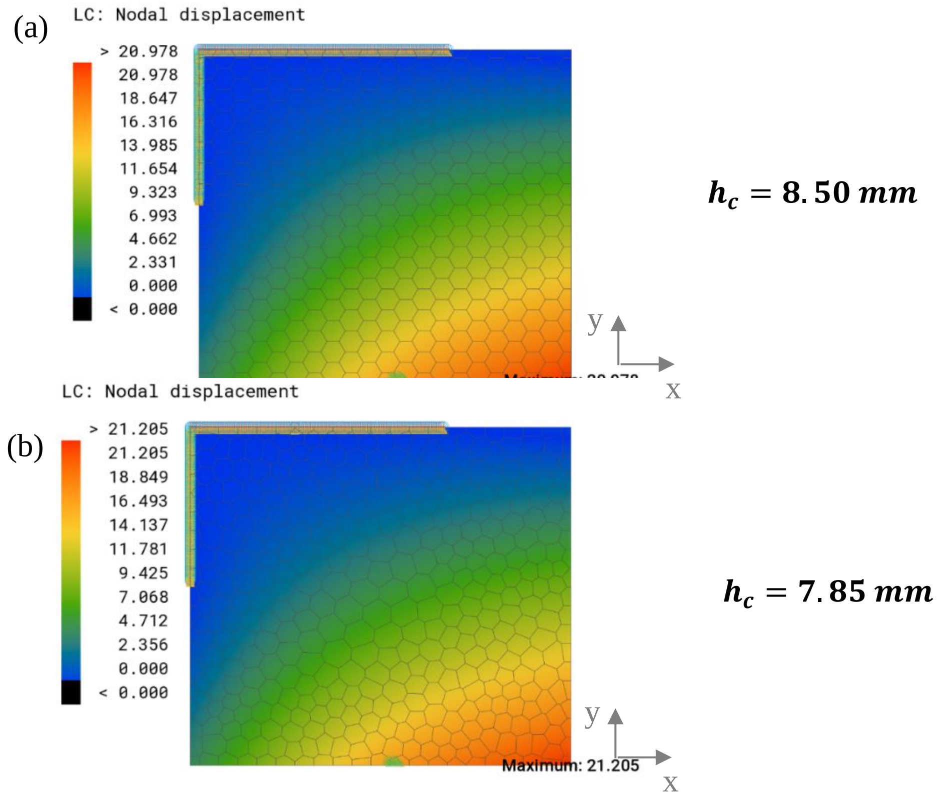

Figure 3.9. The overall displacement plot and maximum overall displacement [mm] of (a) the model with uniform hexagons with $s_c = 11$ (b) the model with irregular polygons of $d_c = 11$ on the bottom. The rib height h_c shows the uniform height of the comb structures.

Stress adjusted patterns

All three comb patterns that were adjusted to the stress field, showed a size gradient with smaller combs in the areas of high stress and larger combs in the areas of low stress (Figure 3.10). The combs in pattern A showed a locally restricted area of small combs, while the combs in patterns B and C depicted transformed combs in a larger area of the surface. The geometry of individual polygons varied the strongest in pattern C, with some polygons exhibiting rectangular shapes. This resulted in the formation of nearly continuous ribs that extended from the upper edge of the surface to the area of the force application.

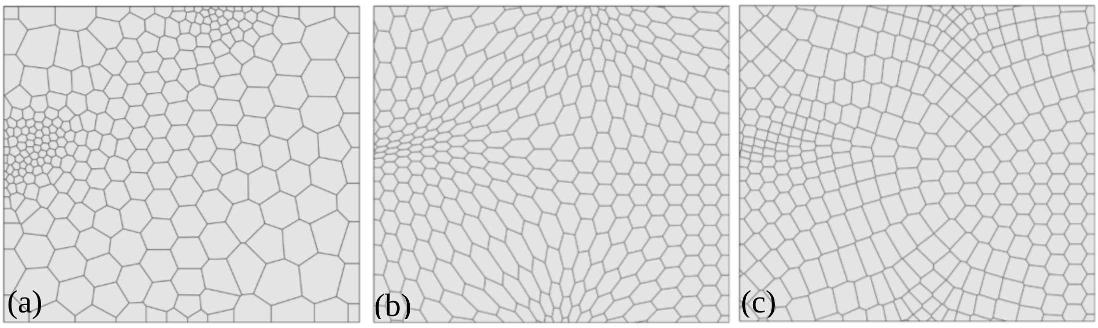

Figure 3.10. Stress-adaptive comb patterns, (a) pattern A: stress-adaptive randomized comb distribution, (b) pattern B: stress-adaptive morphed hexagon combs (c) pattern C: stress-adaptive morphed hexagon centre points with subsequent Voronoi application.

The maximum displacement was the highest in pattern B and the lowest in pattern with 0.66 times the maximum displacement of the uniform hexagonal model with $s_c = 11$ (Table 3.1). The rib height was the highest for pattern A and lower in B and C with almost identical values.

Table 3.1. Maximum overall displacement δ_{max} [mm], maximum displacement normalised to δ_{max} of the hexagonal model with $s_c = 11$ (see Figure 3.9, a) and the rib height h_c [mm] of the three patterns.

Pattern	δ_{max} [mm]	$\delta_{max}/\delta_{max,hexagon}$	h_c [mm]
A	14.80	0.71	10.30
B	19.51	0.93	8.40
C	13.87	0.66	8.48

Sandwich structures

Chosen for the next step was pattern C, where an added sandwich structure decreased the maximum overall displacement of the model for all tested offset distances (Figure 3.11). With an increase in the sandwich offset the maximum displacement decreased further. As the sandwich structure added mass to the model, the rib height was less than in the previous models and decreased with a larger offset. An offset distance of $d_o = 1.5\ mm$ resulted in an error for 3 of the combs with a smaller size, as the offset was too large to create valid edges. Thus, the offset was performed, deleting the three invalid offsets.

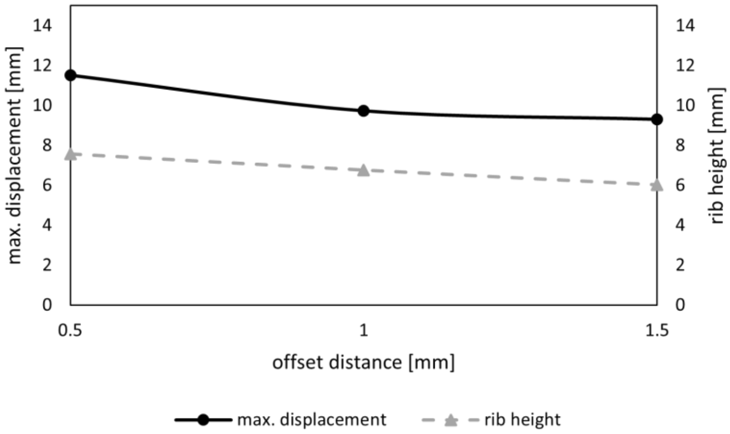

Figure 3.11. Maximum overall displacement [mm] of the model and rib height of the combs [mm], in relationship to the offset distance d_o [mm] of the sandwich surface.

3.2.5 Combined approach: Stress-adaptive sandwich structures

The combined model consisted of pattern C of Figure 3.10, joined with a sandwich pattern with an offset distance of 1.5 mm, which was the largest possible offset in accordance with the comb shapes. Figure 3.12 shows the geometrical features of the combined model. The sandwich structure is indicated in dark grey, the combs in medium grey and the base plate in light grey. The height of the combs was the highest with $h_c = 15\ mm$ around the edges of the support. The corners on the upper left and the lower right showed no combs, which is where the stress in the reference model was close to or equal to 0 MPa.

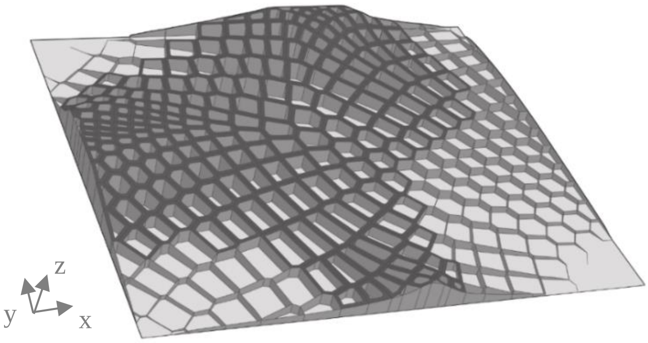

Figure 3.12. Visualisation of the resulting model and its geometrical features. The dark grey areas indicate the sandwich structure, the extruded combs are coloured medium grey, and the base plate is coloured light grey.

A representation of the thicknesses of the optimised model and its displacement is visualized in Figure 3.13. The highest thicknesses of the shell elements were observed in the sandwich structures and the upper areas of the extruded combs. The thickness decreased in the central areas of the combs, which exhibited a minimum thickness value of 0.5 mm. The displacement plot showed a similar distribution as in the other models; however, it exhibited significantly lower maximum overall displacement as the other biomimetic models, with $\delta_{max} = 2.49\,mm$. The combined model depicted $\delta_{max} = 5.68\,mm$ without applying the thickness optimisation (Appendix, A.6).

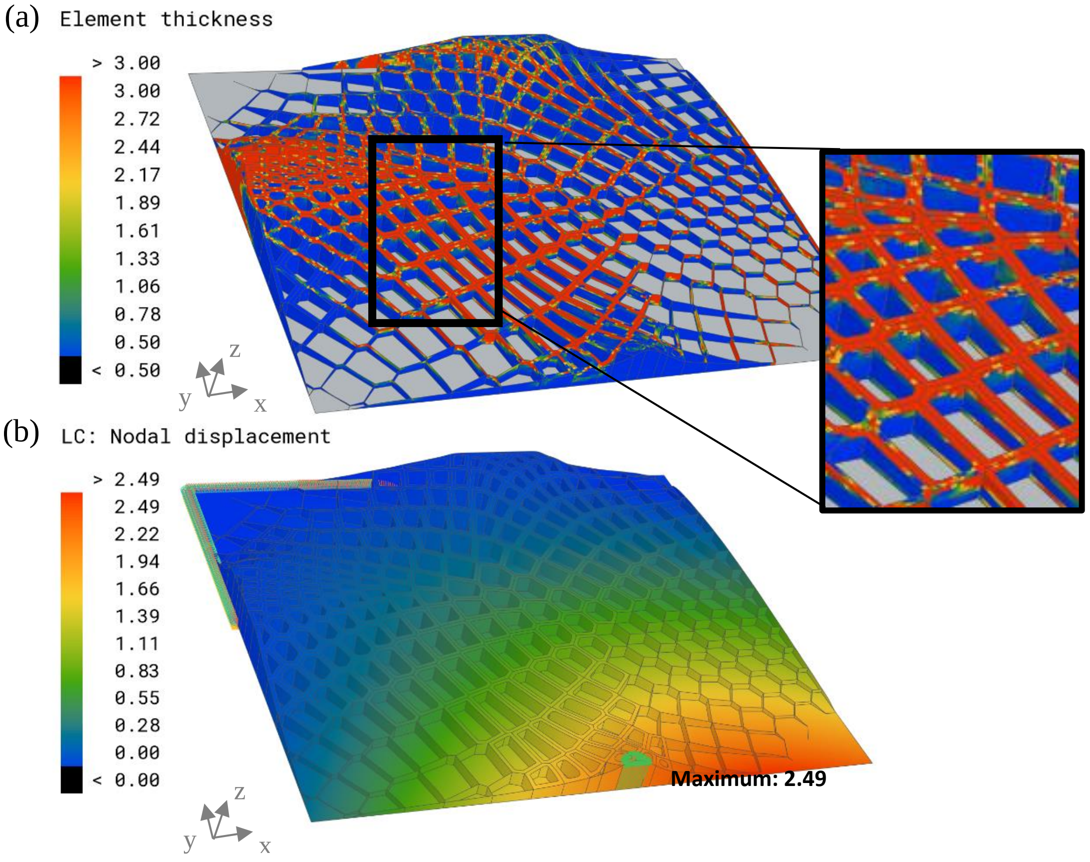

Figure 3.13. (a) Element thickness plot [mm] of the optimised model and a detailed view displayed on the right. Parts excluded from the optimisation are indicated in grey. (b) Overall displacement plot and maximum overall displacement [mm] of the combined model.

Based on these results, elliptical holes were cut into the combs, which have an area A larger than 30 mm^2. The resulting model was similar to the previous one but exhibited higher ribs and the reduced A in the combs (Figure 3.14).

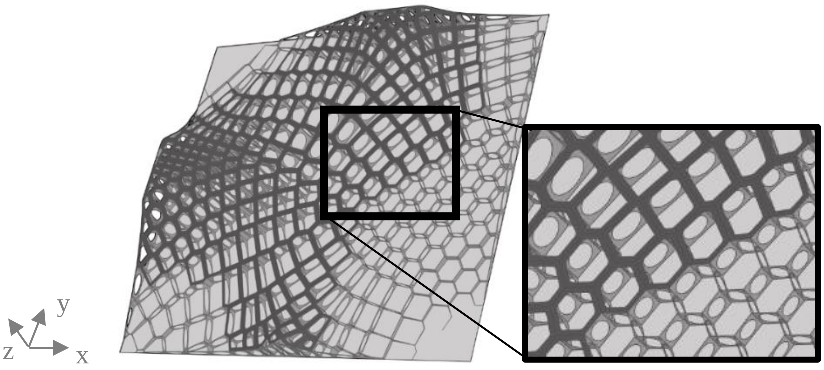

Figure 3.14. Visualisation of the improved combined model, with reduced material in the combs and an increased rib height. The dark grey areas indicate the sandwich structure, the extruded combs are coloured medium grey, and the base plate is coloured light grey.

The distribution of element thickness and the displacement of the improved model showed similarities to the previous model (Figure 3.15). The addition of the plate to the thickness optimisation resulted in a thickening of the plate in the central areas and in the lower right corner, where the maximum displacement was observed in most models. By applying the improvements, δ_{max} was further reduced to 2.03 mm.

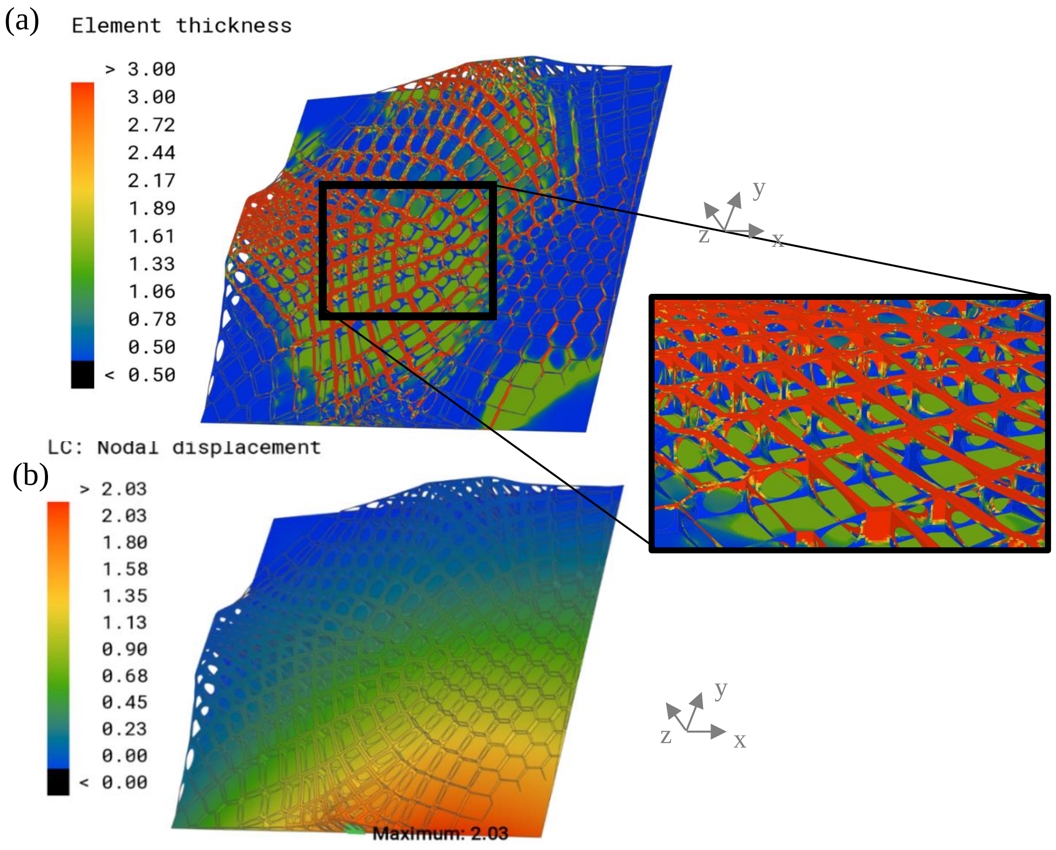

Figure 3.15. (a) Element thickness plot [mm] of the improved model and a detailed view displayed on the right. (b) Overall displacement plot and maximum overall displacement [mm] of the improved combined model.

3.3 Comparison of the presented approaches

From the comparative analysis of the results, the diagram depicted in Figure 3.16 was derived. The diagram illustrates the maximum overall displacement of the key models, normalised to the maximum overall displacement of the reference plate. Since all models had the same mass, with deviations of less than 0.1 %, the displacement was comparable. All the models developed within this study exhibited better values for the target variable compared to the reference model. Among the created models, the simple uniform hexagonal model demonstrated the highest maximum displacement. Subsequent models, incorporating more adjustments, showed a gradual reduction in maximum displacement, with the improved combined model displaying the lowest maximum displacement among the bio-inspired models, which measured less than 7 % of the reference model. The thickness-optimised model generally exhibited the lowest maximum overall displacement, at approximately 3 % of the reference model. The rib model fell within the intermediate range, with approximately 23 % of the maximum displacement of the reference model.

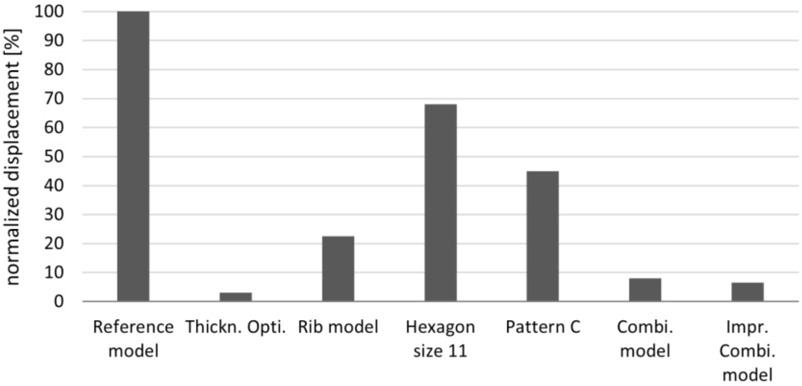

Figure 3.16. A comparative representation of the maximum displacement [%] of the key models normalised to δ_{max} of the reference model.

3.4 Variation of the boundary conditions

The proposed approach was successfully implemented on the non-planar reference surface. The configuration resulted in a von Mises stress distribution, as depicted in Figure 3.17, characterised by a prominent peak observed around the lower edge. Consequently, the generated model exhibited an enhanced rib height in this region, along with smaller deformed combs. Notably, the sandwich structure was observed in proximity to the same area and extended towards the centre of the surface. Thus, the upper edge displayed lower stress values, leading to reduced rib heights and an absence of the sandwich structure.

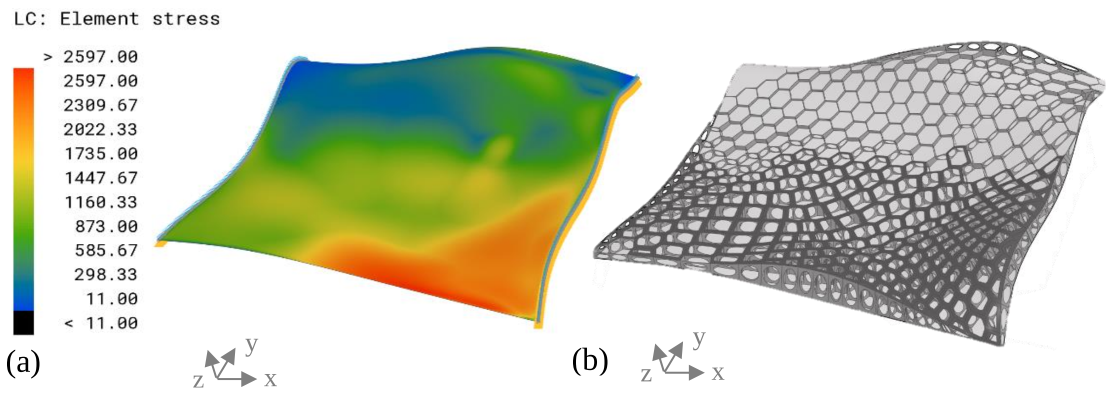

Figure 3.17. (a) von Mises stress distribution [MPa] in the non-planar reference surface resulting from configuration 2. (b) Visualisation of the improved combined model approach applied to the non-planar surface. The dark grey areas indicate the sandwich structure, the extruded combs are coloured medium grey, and the base plate is light grey.

The non-planar reference surface with a thickness of $t = 2.65$ mm showed a maximum displacement on the lower edge of $\delta_{max} = 38.66\ mm$ (Figure 3.18). The model with the implemented thickness optimisation, had a lower displacement of $\delta_{max} = 2.33\ mm$ and the displacement was more evenly distributed throughout the model. The maximum overall displacement of the combined model was $\delta_{max} = 2.63\ mm$ appearing on the opposite side compared to the non-planar reference model.

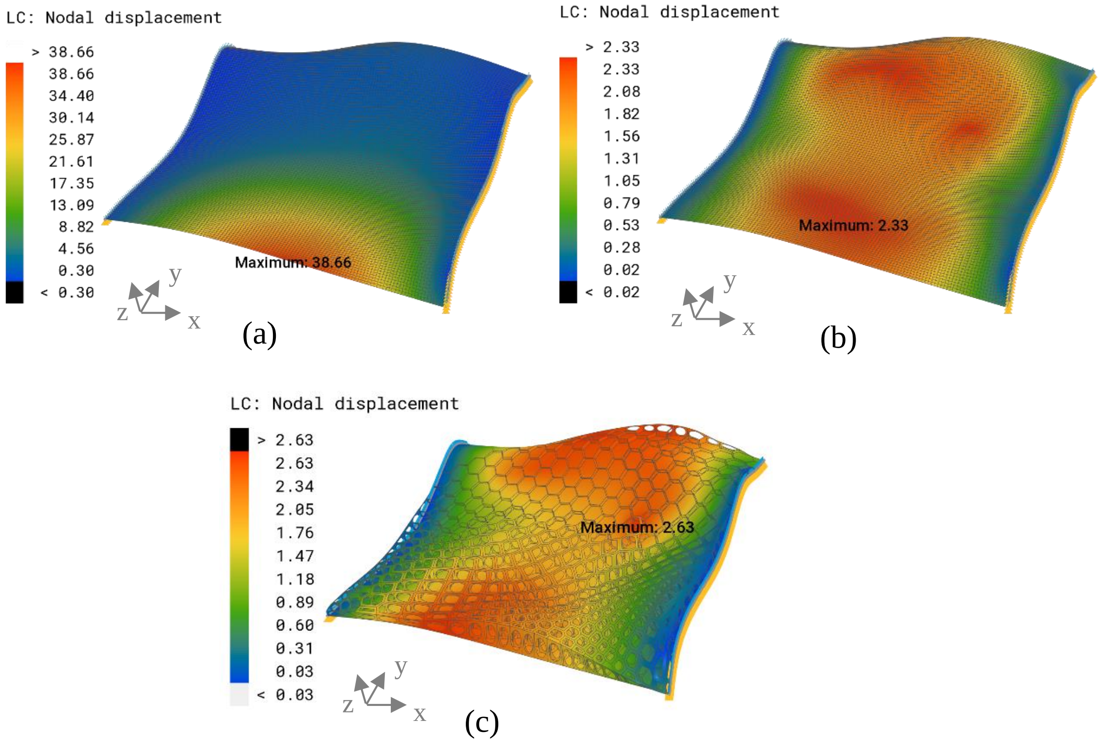

Figure 3.18. Overall displacement plot and maximum overall displacement [mm] of (a) the non-planar reference surface (b) the thickness-optimised model (c) the improved combined model.

The thickness optimisation of the non-planar surface resulted in strut-like structures with the most prominent one extending on the lower edge connecting the supported edges (Figure 3.19, a). The optimised combined model exhibited a similar thickness distribution as in the planar model. Higher thicknesses were observed in the sandwich structure and the upper parts of the combs (Figure 3.19, b).

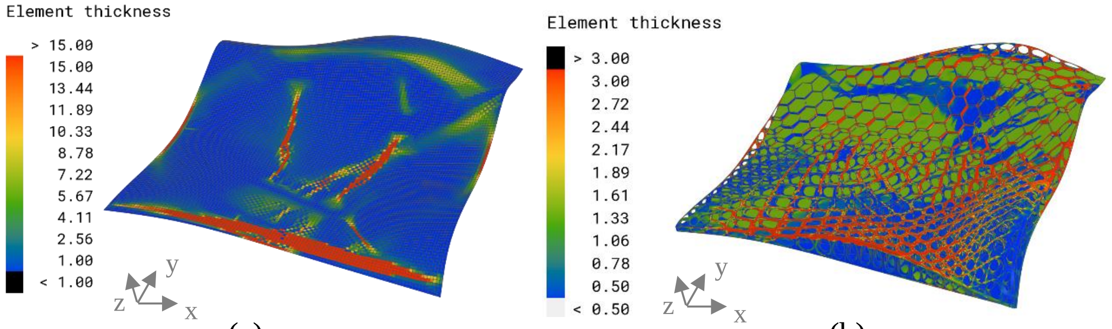

(a) (b)

Figure 3.19. Element thickness plot [mm] of (a) the thickness optimised plate and (b) the combined model of the non-planar plate.

4 Discussion

4.1 Characterisation of diatom frustules

4.1.1 Microscopic analysis

The microscopic analysis with the presented techniques proofed to be suitable for this study. Images taken with the light microscope give a first impression of the features and the size of the diatom, but do not allow a detailed analysis of the frustules. SEM and CLSM are powerful techniques for imaging diatoms, providing high-resolution images of the cell wall structure. CLSM provides a 3D view of the sample and is thus better suited to obtain an impression of the morphology. SEM allows for the visualization of specific structures within the frustule. CLSM and SEM complement each other and enable the understanding of structures in 3D with a high level of detail. Particularly smaller diatoms, as some species of the genus *Pinnularia*, make the use of SEM inevitable. The use and combination of these techniques has advanced the comprehensive analysis of diatom frustules.

4.1.2 Characterisation of structural features

Identified features

For this study, it was chosen to abstract the morphological features individually, even though they are found in complex combinations in the frustules. It is likely that the frustules of different species co-evolved into different defence strategies, based on their predatory environment and that the variety of feeding strategies from predators make a universal protection impossible (Hamm & Smetacek, 2007). This makes it difficult to analyse the defence strategies of the frustules as a whole, thus, the here presented approach to examine the geometric features of the frustules individually is more suitable and feasible.

The morphological features observed in diatom frustules, including combs, irregular and regular hexagons, rib and strut structures, and hierarchical arrangements, hold significant interest as surface stiffeners. These structural mechanical features lead to surface stiffening, increasing the rigidity and thus the load-bearing capability of the diatom while using minimal material (Hamm & Smetacek, 2007). The combs, hexagons, and size gradients observed particularly in centric diatom frustules distribute stresses and strains effectively, enhancing overall stiffness. The walls of the areolae of many diatoms, particularly centric diatoms, form an I-cross-section with the velum and the foramen. This shape is a favourable cross-section regarding the second moment of area I. Compared to a simple rectangular cross-section, this results in an increased I, which simultaneously increases the bending stiffness (Gross et al., 2006).

Additionally, this can be observed in costae, which are often thickened at the naked edge and combined with the basal layer results in an I-beam. These rib and strut structures, predominantly found in pennate diatoms, act as reinforcing elements, minimizing deformations and stress concentrations (Zglobicka & Kurzydlowski, 2022; Hamm, 2005). Costae surround fragile areas to deflect the stress concentrations and avoid crack propagation. Pennate diatoms likely have more prominent strut and rib-like support structures, due to the elongated shape and the raphe, which is present in many genera.

Motile diatoms have a raphe which is necessary for locomotion. Mechanically the raphe is a very fragile region making the frustule more prone to failure, which makes supporting structures crucial. Diatoms with a raphe have more strut-like transapical structures, reinforcing the raphe canal (Hamm, 2005). The sternum, surrounding the raphe, is usually thickened, giving an additional support to the raphe by an increased material accumulation. The rounded structures with no hard ends are important for an equal distribution of stress, which makes the reinforcing structures like costae an important factor to prevent crack propagation.

Many centric diatoms lack costae and mainly consist of comb structures, however genera such as *Arachnoidiscus* constitute the exception. The reason for this is unclear, *Arachnoidiscus* is a relatively large epiphytic genus (Round et al., 1990), the individuals analysed in this study showed diameters of up to 234 µm. The costae might be an extra structural support for the large cell, or an adaptation to the epiphytic lifestyle and predation by snails. Studies showed that *Arachnoidiscus* sp. compared to other centric diatoms are more resilient to applied forces, imitating the attacks by different predators (Wullenweber, 2013). Furthermore, the presence of hierarchical structures, combining microscale combs with macroscale rib and strut formations, contributes to enhanced mechanical properties.

Some observed attributes were not considered for modelling in this work. The focus was set on identifying stiffening structures. Aspects such as undulations, which were observed in the valve of *Actinoptychus* sp. and the girdle region of *Terpsinoë* sp., influence the basic shape of the valves and were thus neglected. It must be stated that these likely also contribute to an increased stiffness, by increasing the distance to the neutral fibre of the valve or the girdle region.

It is evident that there is a high diversity in diatom morphologies, but that the individual features contributing to the mechanical performance of the frustule are similar and can be found in all studied genera, in different combinations. These observed characteristics resemble several lightweight designs used in engineering solutions. I- and T-Beams are commonly used especially in architecture as for their favourable mechanical properties (Kooistra & Pohl, 2015). As well as sandwich-structured panels with two stiff outer layers, that are connected by a low-strength core, often shaped like combs. Overall, the identified morphological features in diatom frustules provide intriguing possibilities for the design of surface stiffeners, merging efficiency, mechanical reinforcement, and a lightweight architecture.

4.2 Development of surface stiffening structures

Rib approach

The attempt to build an automated workflow in Synera, that generates ribs, based on a stress field was not successful. The approach was thus altered and consisted of many different steps, and a manual construction of the ribs. This is more time consuming and difficult to replicate, as it requires knowledge in topology optimisation, CAD and parametric design and the use of a variety of different software. A new software update of Synera recently enabled the extraction of load paths in a model. This feature could make an automated improved version of this workflow possible.

The displacement was improved compared to the reference model, but the combined model outperformed it. It must be considered that no thickness optimisation was performed, as this manual nature of the rib approach already contained many steps in different software, which are very time-consuming. Furthermore, no stiffening structures are evident in the area, where the maximum displacement is observed. This might be improved, by increasing the area that exhibits the comb structures and including the overall displacement plot as a reference for the placement of ribs.

Comb approach

The results of the comb size and offset study, both revealed that displacement is reduced by placing material further away from the neutral fibre of a structure. The reduced deflection observed in the conducted studies aligns with the previously discussed analysis of diatom frustules. The cross-section of an I-beam has a higher second moment of area than a rectangular cross-section or a T-beam (Gross et al., 2006), thus the models with a sandwich structure had a lower deflection than the models without. The more the material is located at the maximum possible distance from the centroid of the cross-section, such as in the form of a sandwich structure and increased rib heights, the larger the second moment of area and the higher the stiffness. The abstracted principles regarding the increase of the second moment of area, prove to be reliable in enhancing the stiffness of a surface.

Comparing the irregular polygon pattern, with the regular hexagonal pattern, no significant difference could be detected in the displacement of the models. It was thought that the regular hexagonal shape would be more efficient, as it might distributes stress more evenly than irregular polygons. Furthermore, the use of a hexagon pattern, also called hexagonal packing, is the most efficient in minimizing the perimeter to area ratio, while maximizing density. Thus, it is often observed in nature. The insignificant difference in δ_{max} of the two models is likely due to the applied load case, which results in compression and tensile stress. As mentioned before, the comb walls contribution to the load bearing is thought to be less important. The comb pattern will likely have a more significant influence for other load cases, such as in-plane loading, which create shear stress, which is assumed to be carried by the comb structures. Further simulations are needed to analyse this hypothesis.

The developed adaptive patterns further decreased the displacement, due to a more particular material distribution, which better dissipated the emerging stress peaks, through an accumulation of material in critical areas. Pattern C might have had the lowest maximum overall displacement because the performed modification of the pattern resulted in almost continuous lines of the combs, that expand from the support areas to the load bearing area. These continuous ribs likely deflected the stress better, which resulted in a lower displacement.

Combined approach

Evidently, the individual features made significant contributions toward reducing displacement. However, the greatest efficiency was achieved through their combined implementation in the form of the combined model. Moreover, the exploration of thickness optimisation on the combined model yielded further decrease in maximum overall displacement. The implementation of thickness optimisation aligns with the intrinsic attributes of natural structures, such as found in diatom frustules, where non-uniform thicknesses are observed, leading to optimised material arrangements. This optimisation strategy also contributes to the reinforcement of uniform stress distribution by strategically reducing thickness in regions marked by low stress values.

It became evident that the minimal thickness allocation of the improved combined model appeared in the comb walls. This revelation underscores their limited significance in bearing loads during a bending load scenario. Notably, this observation echoes the findings of Aitken et al. (2016), affirming that walls in certain diatom species primarily function to deflect shear forces rather than withstand bending loads. This insight implies that the comb walls serve to maintain separation between the base layer and the sandwich construction, while their importance might become more pronounced in other load cases, such as in-plane scenarios. Given that Coscinodiscus frustules often encounter compressive and tensile forces around the girdle region, the comb walls may play an important role in mitigating these stresses (Aitken et al., 2016). Thus, the improved combined approach involving cutouts could potentially lead to increased displacement during in-plane load cases, as the structural significance of the comb walls might intensify under such conditions.

The computational time required for the improved combined model is notable, as the algorithm applied to this complex structure demands several hours for completion. Despite this, the initial establishment of the workflow was time-consuming, yet its subsequent application to novel models or boundary conditions is fast and uncomplicated, requiring a few minutes for adjustments.

4.3 Comparison of the presented approaches

Overall, the inclusion of ribbing structures, resembling those found in diatoms, consistently outperformed the simple strategy of uniformly thickening the reference plate. This observation aligns with the findings by Hamm (2003), who showed that thickened frustules with removed ribbing structures had a 70 % higher displacement than ribbed models with the same total mass.

Notably the engineering approach proved effective, outperforming the other approaches for load case 1. As a thickness optimisation is directly optimised to fit the given load case, it surpassed the efficacy of the biomimetic solutions. This outcome leaves the question, why a straightforward, thickness-optimised material distribution is not commonly observed in diatom frustules. While this principle is present in certain natural structures like trees or bones, which routinely encounter consistent forces, most living organisms are generalists and must be resilient towards a variety of different load cases. Diatoms serve as a prime example, needing to adeptly manage an array of stressors introduced by various predators.

Technical problems in many cases face a very specific set of forces, such as presented in this study, that diverge from the complex and diverse forces encountered in real-world scenarios. Thus, a thickness optimisation may be more applicable for specific and consistent load cases, as it is specifically adjusted to that set of forces. However, the effectiveness of thickness optimisation declines when confronted with different force dynamics. The combined sandwich approach, as demonstrated, emerges as a highly promising solution, that has room for further improvement. Thus, it can be hypothesized that the biomimetic surface stiffeners are more suitable for complex load cases, as it is a more robust and versatile design, that exhibits resilience across a range of load cases. Further studies with randomized varying forces are necessary to validate this assumption.

When comparing the labour and computational effort of the approaches, the improved combined model was the most time consuming both in creating the workflow as well as in computational effort. The process of the thickness optimization takes the most computational time, especially in the combined models, as the structures are more complex than in the reference plate. The workflow of the combined model took about a month to initially set up and improve, but the subsequent application to a new model only takes a few minutes and about a day to run and create the structure. The rib approach, as it is not an automatic workflow, has to be performed manually each time it is applied to a novel scenario. Thus, the initial setup of the model was faster than for the combined model, with about a week of labour, but the subsequent use is more time intensive and needs knowledge in several different software applications, while the combined model is setup in only one software and runs automatically after inputting the boundary conditions.

Ultimately, this study highlights the potential of diatom-inspired structures to increase stiffness of surfaces. Exemplary applications could be in aerospace engineering, these structures could revolutionize aircraft design by enhancing the durability and efficiency of wings and fuselage panels. Adaptive stiffening structures could be applied in medical devices, such as prosthetics, where a high robustness is required. The parametric design would enable a fast way of creating a personalised design optimally adapted to a patient’s physical characteristics. could be made more robust and long-lasting, adapting to stress patterns within the body. While certain technical applications may favour conventional methods, diatom-inspired stress-adaptive designs show promise for scenarios subjected to varying stresses, necessitating lightweight and robust solutions.

4.4 Variation of the boundary conditions

The alternative configuration showed a decreased difference in maximum overall displacement for the combined model and the thickness optimisation, this could underline the previously introduced hypothesis, that the biomimetic approach is performing better for load cases with more complex conditions and several load cases. The thickness optimisation for load case 1 was specialized for one applied force, thus, it was possible to accumulate a lot of material in one area, making the model perfectly adapted to this specific load bearing. When more complex load cases are apparent, where stress concentrations are present in several different areas of the structure, a simple thickness optimisation might not be sufficient. The material would have to be evenly spread, which results in a lower possible thickness as a high amount of material is accumulated. On the contrary, the diatom-inspired approach, enables the distribution of support structures, with a lower amount of material than a simple thickening. This results in a higher possible height of the structures. As the material has a bigger distance to the neutral fibre of the structure, the second moment of area is higher and thus, increases the stiffness.

The workflow of the improved combined model was robust against the input of a modified load case but had to be adjusted to be applicable to non-planar surfaces. This included the implementation of a section of the workflow, that creates a planar version of the non-planar surface, before continuing with the workflow described for the planar surface. In the final section of the workflow, the created structures were morphed onto the original non-planar surface. To make the workflow applicable to both planar and non-planar surfaces at the same time, a toggle was integrated as a starting parameter, which allows the user to define whether the input surface is planar or not. Thus, the altered workflow is robust against application for other boundary conditions. As no part of the workflow is dependent on the shape of the input surface, it is expected that the workflow is also applicable to non-rectangular surfaces.

4.5 Limitations

Deviations from real-world scenarios may occur during the simulations, the results of numerical calculations are highly dependent on the meshing of the models and, due to the complex geometries resulting from the honeycomb patterns, there may be occasional narrow areas where the elements do not meet the quality criteria. All these aspects can significantly impact the calculations. Additionally, it should be noted that the element type and the interpolation degree of the displacement function can also influence the outcomes. Since the models were computed using shell elements, element overlaps may occur, affecting the transfer of forces between elements and leading to a discrepancy in mass. Given that the same software and setup were used for analysing the models, it is expected that the results are reliable when analysed in relation to each other. Nevertheless, further experiments should be conducted to validate the numerical analysis.

Another limitation is given by the manufacturing. As the presented structures contain sandwich geometries, many manufacturing methods are not suitable, due to the complexity of the geometries. A possibly adequate method could be additive manufacturing, such as selective laser melting, that can be used for metal powders. Another possibility could be the individual manufacturing of the comb core, the sandwich structure and the base plate, subsequently combined with an adhesive method as commonly used for sandwich panels. Adhesive lamination results in a strong bond between the core and the skin layers, which is suitable for lightweight applications.

4.6 Outlook

The positive outcomes of this study, particularly in the augmentation of plate stiffness, provide a solid foundation for subsequent analyses. The current investigation encompassed surface models, with 2D-meshes, characterised by defined edges. A logical progression would involve the creation of comprehensive 3D models. This would enable the modelling with rounded edges, as they are found in diatom frustules. The anticipated result of that modification would be an enhanced stress distribution, and conceivably, a further increase in bending stiffness. However, this step would inevitably demand an increase in labour and computational effort.

The foundation of the presented adaptive model is a stress pattern. This means that the approach relies on a connection between the stress distribution and the displacement. A promising direction for investigation could be to utilize a thickness optimisation in combination with a detailed mesh, instead of the stress field of a reference model. This would allow the obtained thickness values to be converted into a spatial layout and serve as a base to manipulate the adaptive structures. This approach offers the potential to guide the evolution of adaptive structures, without being susceptible to anomalies in the stress distribution. A further step would also be to explore manufacturing of the models and the influence of material properties. This can include comparing the behaviour of different materials and possible manufacturing techniques, such as additive manufacturing.

Applications that call for a surface stiffening often contain areas that should not be altered, as for restrictions regarding the dimensions of the structure in specific regions, or due to areas that connect to other parts. These characteristics could be integrated into the workflow, by defining non-design spaces, that shall be free from stiffening structures.

An alteration of the base plate by including pores could also be considered, if in line with the specific needs of the application. However, attempting to imitate the diatom frustules by cutting the centres of the combs could result in fragile areas with stress concentrations and vulnerability to crack propagation, as observed in frustules, such as in the findings reported by Aitken et al. in 2016. Another idea could be to employ hierarchical structures, involving smaller comb structures within each primary comb. However, it is theorized that their potential to substantially enhance stiffness in the load cases examined in this study might be limited. Instead, their incorporation would primarily introduce additional wall structures that may not significantly contribute to bending stiffness. Although their strategic placement in high-stress zones could be considered, this approach would demand increased material usage, potentially leading to material reduction in other regions. To validate this hypothesis, conducting further simulations is imperative.

Inspired by the architectural features of the costae in *Arachnoidiscus* sp., combining the proposed method of the combined model with larger ribs, such as in the rib model, along main load paths present an interesting approach. A recent software update of Synera is supposed to enable the extraction of the main load paths of a surface. This feature could simplify the implementation of this approach.

Within the realm of optimisation, a possible improvement would involve implementing a thickness optimisation process with the constraint of a single thickness value per surface instead of per element of the mesh. Based on the result of this optimisation, a workflow could be introduced to selectively filter out surfaces assigned the smallest thicknesses and delete them. Alternatively, a topology optimisation could be included before the thickness optimisation, to reduce the number of unloaded surfaces. This strategy enables the elimination of structurally redundant surfaces and potentially improves the principle of consistent stress distribution but also facilitates a basis for more efficient load bearing.

As is evident, this biomimetic method, facilitated through abstraction, provides a foundation for a multitude of potential diatom-inspired designs. If these designs are a potential alternative to common engineering solutions is reliant, among other things, on computational effort and the investment of working hours. Furthermore, this methodology involves a trial-and-error approach due to the sheer volume of possible implementations.

5 Conclusions

The exploration of biomimetic stiffening structures inspired by diatom frustules morphologies has provided valuable insights into the potential of nature-inspired engineering solutions. The primary objective of this study was to ascertain whether the presented innovative approach is a promising alternative of addressing engineering challenges that call for an increase in stiffness. Through analysis and experimentation, it has been demonstrated that the implementation of an adaptive diatom-inspired approach yields notable improvement in bending stiffness, which manifests in a decrease of displacement by about 93 % compared to the reference model with the same total mass.

While the immediate performance of the engineering approach, in this study exemplified by simple thickness optimisation, mechanically outperformed the biomimetic approach, it must be noted that the simulated load cases were very simple and deviate from natural load cases. It is anticipated that the inherent strength of the biomimetic approach will manifest more prominently in intricate load scenarios, comparable to forces that are prominent in the natural world encountered by diatoms. Thus, it can be assumed, that in the face of more complex or variable load cases, that call for robust solutions, the biomimetic methodology will likely surpass the performance of traditional thickness optimisation techniques. The biomimetic approach was successfully automated to a high degree by using parametric design. Therefore, a workflow was created, that is applicable to both planar and non-planar surfaces and adapts to the specific stress distribution of a provided scenario, by only defining some parameters, such as the boundary conditions.

In summation, the findings of this study underline the remarkable potential of diatom frustules as an inspiration for biomimetic engineering. This study thus contributes to the ongoing discourse on nature-inspired solutions and invites further exploration of interdisciplinary methods.

6 References

Aguirre, L. E., Ouyang, L., Elfwing, A., Hedblom, M., Wulff, A., & Inganäs, O. (2018). Diatom frustules protect DNA from ultraviolet light. Scientific reports, 8(1), 5138.

Aitken, Z. H., Luo, S., Reynolds, S. N., Thaulow, C., & Greer, J. R. (2016). Microstructure provides insights into evolutionary design and resilience of Coscinodiscus sp. frustule. Proceedings of the National Academy of Sciences, 113(8), 2017-2022.

Arrieta, J., Jeanneret, R., Roig, P., & Tuval, I. (2020). On the fate of sinking diatoms: the transport of active buoyancy-regulating cells in the ocean. Philosophical Transactions of the Royal Society A, 378(2179), 20190529.

Aurenhammer, F. (1991). Voronoi diagrams—a survey of a fundamental geometric data structure. ACM Computing Surveys (CSUR), 23(3), 345-405.

Baumgart, E. (2000). Stiffness—an unknown world of mechanical science. Injury, 31(Suppl 2), B14-23.

Bendsoe, M. P., & Sigmund, O. (2003). Topology optimisation: theory, methods, and applications. Springer Science & Business Media.

Berg, H. C., & Purcell, E. M. (1977). Physics of chemoreception. Biophysical journal, 20(2), 193-219.

Breish, F., Hamm, C., & Kienzler, R. (2023). Diatom-inspired stiffness optimisation for plates and cellular solids. Bioinspiration & Biomimetics, 18(3), 036004.

Christensen, P. W., & Klarbring, A. (2008). An introduction to structural optimisation (Vol. 153). Springer Science & Business Media.

Coenders, J. L. (2021). Next generation parametric design. Journal of the International Association for Shell and Spatial Structures, 62(2), 153-166.

Cvjetinovic, J., Luchkin, S. Y., Statnik, E. S., Davidovich, N. A., Somov, P. A., Salimon, A. I., ... & Gorin, D. A. (2023). Revealing the static and dynamic nanomechanical properties of diatom frustules—Nature's glass lace. Scientific Reports, 13(1), 5518.

Darwin, C. (1859) On the origin of species by means of natural selection, or, The preservation of favoured races in the struggle for life. D. Appleton and Company.

De Stefano, L., De Stefano, M., Maddalena, P., Moretti, L., Rea, I., Mocella, V., & Rendina, I. (2007a). Playing with light in diatoms: small water organisms with a natural photonic crystal structure. In Photonic Materials, Devices, and Applications II (Vol. 6593, pp. 305-313). SPIE.

De Stefano, L., Rea, I., Rendina, I., De Stefano, M., & Moretti, L. (2007b). Lensless light focusing with the centric marine diatom Coscinodiscus walesii. Optics Express, 15(26), 18082-18088.

De Tommasi, E., Gielis, J., & Rogato, A. (2017). Diatom frustule morphogenesis and function: a multidisciplinary survey. Marine genomics, 35, 1-18.

Desclés, J., Vartanian, M., El Harrak, A., Quinet, M., Bremond, N., Sapriel, G., ... & Lopez, P. J. (2008). New tools for labeling silica in living diatoms. New Phytologist, 177(3), 822-829.

Falciatore, A., & Bowler, C. (2002). Revealing the molecular secrets of marine diatoms. Annual review of plant biology, 53(1), 109-130.

Falciatore, A., d'Alcalà, M. R., Croot, P., & Bowler, C. (2000). Perception of environmental signals by a marine diatom. Science, 288(5475), 2363-2366.

Fattahi, F., Hashemian, E., & Rezaie, A. (2013). Emergent pattern generation method.

Finkel, Z. V., & Kotrc, B. (2010). Silica use through time: macroevolutionary change in the morphology of the diatom fustule. Geomicrobiology Journal, 27(6-7), 596-608.

Garcia, A. P., & Buehler, M. J. (2010). Bioinspired nanoporous silicon provides great toughness at great deformability. Computational Materials Science, 48(2), 303-309.

Gebeshuber, I. C., & Crawford, R. M. (2006). Micromechanics in biogenic hydrated silica: hinges and interlocking devices in diatoms. Proceedings of the Institution of Mechanical Engineers, Part J: Journal of Engineering Tribology, 220(8), 787-796.

Gebeshuber, I. C., Kindt, J. H., Thompson, J. B., Del Amo, Y., Stachelberger, H., Brzezinski, M. A., ... & Hansma, P. K. (2003). Atomic force microscopy study of living diatoms in ambient conditions. Journal of Microscopy, 212(3), 292-299.

Gebeshuber, I. C., Thompson, J. B., Del Amo, Y., Stachelberger, H., & Kindt, J. H. (2002). In vivo nanoscale atomic force microscopy investigation of diatom adhesion properties. Materials Science and Technology, 18(7), 763-766.

Goessling, J. W., Su, Y., Cartaxana, P., Maibohm, C., Rickelt, L. F., Trampe, E. C., ... & Kühl, M. (2018). Structure-based optics of centric diatom frustules: modulation of the in vivo light field for efficient diatom photosynthesis. New Phytologist, 219(1), 122-134.

Goessling, J. W., Su, Y., Maibohm, C., Ellegaard, M., & Kühl, M. (2019). Differences in the optical properties of valve and girdle band in a centric diatom. Journal of the Royal Society Interface Focus, 9(1), 20180031.

Gokhale, N. S. (2008). Practical finite element analysis. Finite to infinite.

Gross, D., Hauger, W., Schnell, W., Schröder, J., & Wall, W. A. (Eds.). (2006). Technische Mechanik: Band 1: Statik [Technical Mechanics: Edition 1: Statics]. Berlin, Heidelberg: Springer Berlin Heidelberg.

Gutiérrez, A., Guney, M. G., Fedder, G. K., & Dávila, L. P. (2018). The role of hierarchical design and morphology in the mechanical response of diatom-inspired structures via simulation. Biomaterials science, 6(1), 146-153.

Haeckel, E. (2012). Art forms in nature. Courier Corporation.

Hamm, C. E. (2005). The evolution of advanced mechanical defenses and potential technological applications of diatom shells. Journal of Nanoscience and Nanotechnology, 5(1), 108-119.

Hamm, C. E., Merkel, R., Springer, O., Jurkojc, P., Maier, C., Prechtel, K., & Smetacek, V. (2003). Architecture and material properties of diatom shells provide effective mechanical protection. Nature, 421(6925), 841-843.

Hamm, C., & Smetacek, V. (2007). Armor: why, when, and how. In Evolution of primary producers in the sea (pp. 311-332). Academic Press.

Harding, J. E., & Shepherd, P. (2017). Meta-parametric design. Design Studies, 52, 73-95.

Hartmann, F., & Katz, C. (2004). Structural analysis with finite elements. Springer Science & Business Media.

Iler, K. R. (1979). The chemistry of silica. Solubility, polymerization, colloid and surface properties and biochemistry of silica.

Irwin, A. J., Finkel, Z. V., Schofield, O. M., & Falkowski, P. G. (2006). Scaling-up from nutrient physiology to the size-structure of phytoplankton communities. Journal of plankton research, 28(5), 459-471.

Jantschke, A., Fischer, C., Hensel, R., Braun, H. G., & Brunner, E. (2014). Directed assembly of nanoparticles to isolated diatom valves using the non-wetting characteristics after pyrolysis. Nanoscale, 6(20), 11637-11645.

Kakizaki, E., Kozawa, S., Sakai, M., & Yukawa, N. (2011). Numbers, sizes, and types of diatoms around estuaries for a diatom test. The American Journal of Forensic Medicine and Pathology, 32(3), 269-274.

Kooistra, W. H., & Pohl, G. (2015). Diatom frustule morphology and its biomimetic applications in architecture and industrial design. Evolution of Lightweight Structures: Analyses and Technical Applications, 75-102.

Kooistra, W. H., Gersonde, R., Medlin, L. K., & Mann, D. G. (2007). The origin and evolution of the diatoms: their adaptation to a planktonic existence. Evolution of primary producers in the sea, 207-249.

Lee, G. (2012). Introduction to Meshing. In Altair University: Student Guide (pp. 79-102).

Losic, D., Mitchell, J. G., & Voelcker, N. H. (2006). Fabrication of gold nanostructures by templating from porous diatom frustules. New Journal of Chemistry, 30(6), 908-914.

Lu, J., Sun, C., & Wang, Q. J. (2015). Mechanical simulation of a diatom frustule structure. Journal of Bionic Engineering, 12(1), 98-108.

Maier, M., Siegel, D., Thoben, K. D., Niebuhr, N., & Hamm, C. (2013). Transfer of natural micro structures to bionic lightweight design proposals. Journal of Bionic Engineering, 10(4), 469-478.

Mattheck, C., & Mattheck, C. (1998). The Right Load Distribution: The Axiom of Uniform Stress and Tree Shape. Design in Nature: Learning from Trees, 53-114.

Mcheik, A., Cassaignon, S., Livage, J., Gibaud, A., Berthier, S., & Lopez, P. J. (2018). Optical properties of nanostructured silica structures from marine organisms. Frontiers in Marine Science, 5, 123.

McLaughlin, R. B. (2012). An introduction to the microscopical study of diatoms. Edited by John Gustav Delly&Steve Gill.

Monedero, J. (2000). Parametric design: a review and some experiences. Automation in construction, 9(4), 369-377.

Nachtigall, W. (2003). Bionik: Grundlagen und Beispiele für Ingenieure und Naturwissenschaftler. Springer-Verlag.

Nachtigall, W. (2010). Bionik als Wissenschaft: Erkennen-Abstrahieren-Umsetzen [Research-Abstraction-Implementation]. Springer-Verlag.

Nachtigall, W., & Pohl, M. (2015). Biomimetics: Biologically Inspired Technologies. CRC Press.

Pančić, M., Torres, R. R., Almeda, R., & Kiørboe, T. (2019). Silicified cell walls as a defensive trait in diatoms. Proceedings of the Royal Society B, 286(1901), 20190184.

Pegg, E. C., Murray, D. W., Pandit, H. G., O’Connor, J. J., & Gill, H. S. (2013). Fracture of mobile unicompartmental knee bearings: a parametric finite element study. Proceedings of the Institution of Mechanical Engineers, Part H: Journal of Engineering in Medicine, 227(11), 1213-1223.

Pondaven, P., Gallinari, M., Chollet, S., Bucciarelli, E., Sarthou, G., Schultes, S., & Jean, F. (2007). Grazing-induced changes in cell wall silicification in a marine diatom. Protist, 158(1), 21-28.

Qin, T., Gutu, T., Jiao, J., Chang, C. H., & Rorrer, G. L. (2008). Photoluminescence of silica nanostructures from bioreactor culture of marine diatom Nitzschia frustulum. Journal of nanoscience and nanotechnology, 8(5), 2392-2398.

Raphael, B., & Smith, I. F. (2003). Fundamentals of computer-aided engineering. John wiley & sons.

Raven, J. A., & Waite, A. M. (2004). The evolution of silicification in diatoms: inescapable sinking and sinking as escape?. New phytologist, 162(1), 45-61.

Renaudie, J. (2016). Quantifying the Cenozoic marine diatom deposition history: links to the C and Si cycles. Biogeosciences, 13(21), 6003-6014.

Round, F. E., Crawford, R. M., & Mann, D. G. (1990). Diatoms: biology and morphology of the genera. Cambridge university press.

Rozvany, G. I., Zhou, M., & Birker, T. (1992). Generalized shape optimisation without homogenization. Structural optimisation, 4, 250-252.

Ryther, J. H., & Guillard, R. R. L. (1962). Studies of marine planktonic diatoms: II. Use of Cyclotella nana Hustedt for assays of vitamin B12 in sea water. Canadian Journal of Microbiology, 8(4), 437-445.

Shigley, J. E., Mitchell, L. D., & Saunders, H. (1985). Mechanical engineering design.

Svetličić, V., Žutić, V., Pletikapić, G., & Radić, T. M. (2013). Marine polysaccharide networks and diatoms at the nanometric scale. International Journal of Molecular Sciences, 14(10), 20064-20078.

Topal, E., Rajendran, H., Zgłobicka, I., Gluch, J., Liao, Z., Clausner, A., ... & Zschech, E. (2020). Numerical and experimental study of the mechanical response of diatom frustules. Nanomaterials, 10(5), 959.

Wullenweber, M. S. (2013). Funktionelle Morphologie von Diatomeenschalen in Ökosystemen [Functional morphology of diatom frustules in ecosystems]. [Bachelor‘s thesis, University of Hamburg]. Epic AWI. https://epic.awi.de/view/creators/Wullenweber=3AMaike_Sophie=3A=3A.default.html

Young, J. R., & Geisen, M. (2002). Xenospheres-associations of coccoliths resembling coccospheres. Journal of Nannoplankton Research, 24, 27-35.

Zgłobicka, I., & Kurzydłowski, K. J. (2022). Multi-length scale characterisation of frustule showing highly hierarchal structure in the context of understanding their mechanical properties. Materials Today Communications, 33, 104741.

7 Appendix

A.1 Diatom morphology and glossary

Figure A.1 shows some of the terms regarding diatom morphology on the example of *Gomphonema* sp. and *Arachnoidiscus* sp. Additional terms used in this study are listed with a definition in Table A.1.

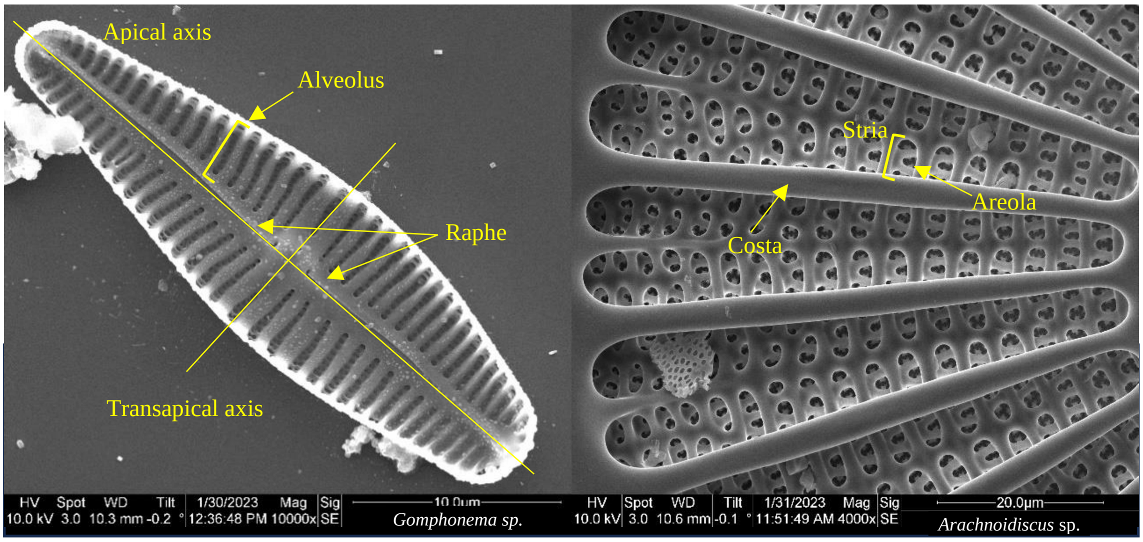

Figure A.1. (a) *Gomphonema* sp. (b) Excerpt of a frustule of *Arachnoidiscus* sp.

Table A.1. Terms used when describing diatom morphology and their definitions.

Term	**Definition**
Areola	One pore in a row of a stria, pore, often polygon-shaped of a centric diatoms valve face
Alveolus	An elongated chamber that forms a whole stria or part of it
Apical axis	The long axis of the valve face of a pennate diatom
Costa, pl. Costae	Elongated thickening of the valve, often parallel to striae
Stria, pl. Striae	A groove that contains a row of areolae, alveoli or a single alveolus
araphid	Diatoms that have no raphe system
raphe	Slit in the silica cell wall composed of one or two branches
monoraphid	A raphe is only present in one valve, the other one is rapheless
biraphid	Having a raphe on both valves of the frustule
sternum	Thickened silica element often positioned along the apical axis. It often contains the raphe
Foramen	Large opening of a chambered areola

Cribellum	Punctured sieve-like layer outside of the velum
Axial costa	A costa positioned on the apical axis of the valve face
undulate	Having the shape of a wave, forming crests and troughs
Fibula	Internal bar or strut supporting the raphe canal
Cribrum	A velum that is reticulate or has arranged pores
velum	Thin porous layer occluding an areola and opposing the foramen
uniseriate	A stria consisting of only one row of areolae

A.2 Complete list of diatom genera identified in this study

An overview of the identified genera in this study is given in Table A.2. Information regarding the environment of the genera is based on Round et al. (1990) and the general morphology was derived from https://diatoms.org (14.07.2023)

Table A.2. Complete list of the identified genera in this study, including their general morphological category and common environments.

Genus	Environment	General morphology
Actinoptychus	marine	Centric
Arachnoidiscus	marine	Centric
Caloneis	marine, brackish, fresh, terrestrial	Symmetric Biraphid
Cymatopleura	marine, brackish, fresh	Surirelloid
Cymbella	fresh	Asymmetric Biraphid
Fragilariopsis	marine	Biraphid
Gomphonema	marine, brackish, fresh	Asymmetric Biraphid
Pinnularia	marine, brackish, fresh, terrestrial	Symmetric Biraphid
Porosira	marine	Centric
Rhaphoneis	Marine, fresh	Araphid
Stephanodiscus	fresh	Centric
Stephanopyxis	marine	Centric
Surirella	marine, brackish, fresh, terrestrial	Surirelloid
Tabellaria	Marine, fresh	Araphid
Terpsinoë	marine, brackish, fresh	Centric
Thalassiosira	marine, brackish, fresh	Centric
Ulnaria	marine, brackish, fresh	Araphid

A.3 Additional images taken with SEM

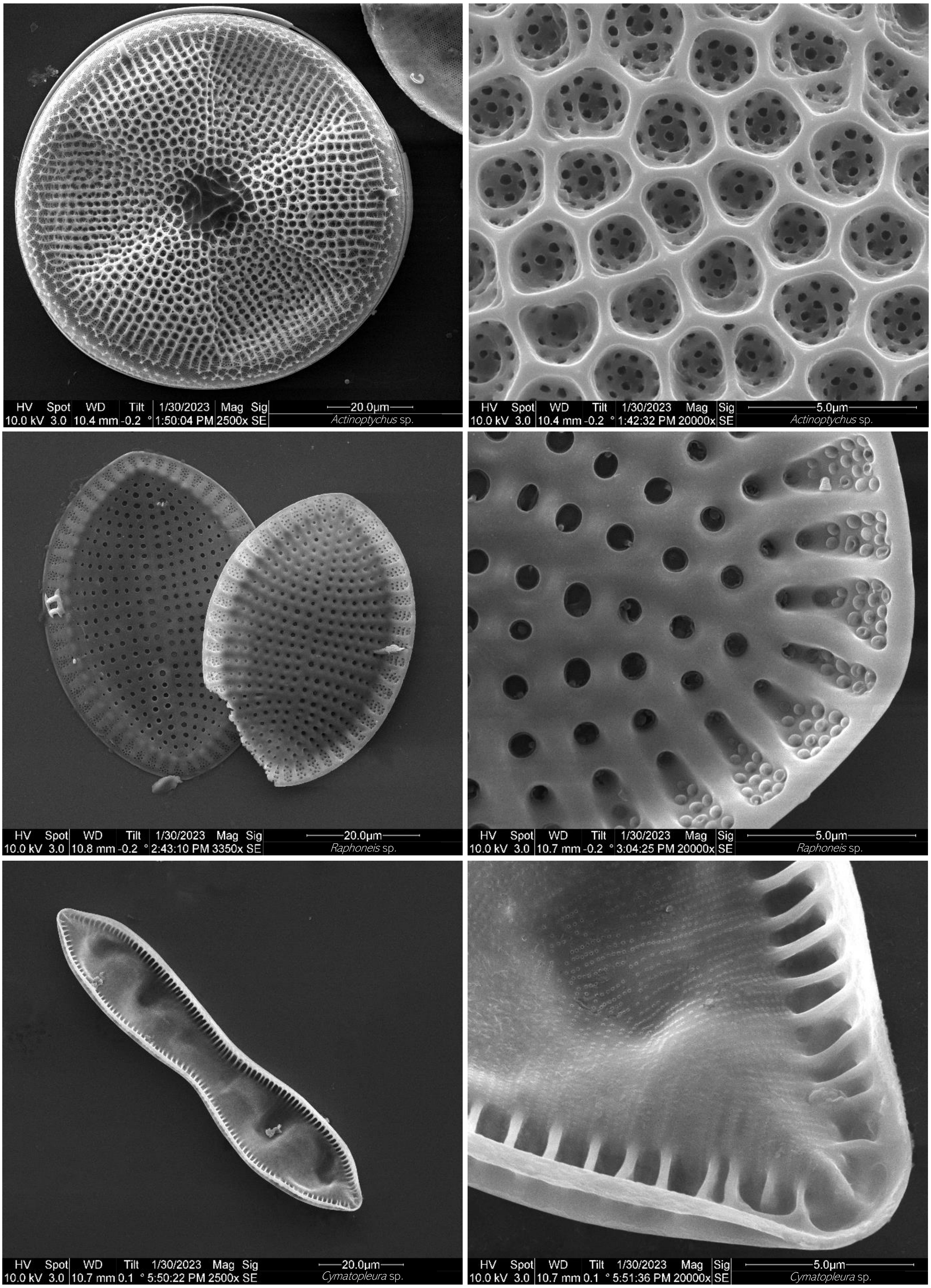

Figure A.3. SEM images of several genera. The genus and the details of the image generation are depicted on the bottom.

A.4 Rib model, Topology optimisation

As a base for the rib model three topology optimisations were performed. Figure A.4 displays the resulting element density plots for a remaining Area A_r of 15 % and 20 %. These plots were not used for the creation of ribs.

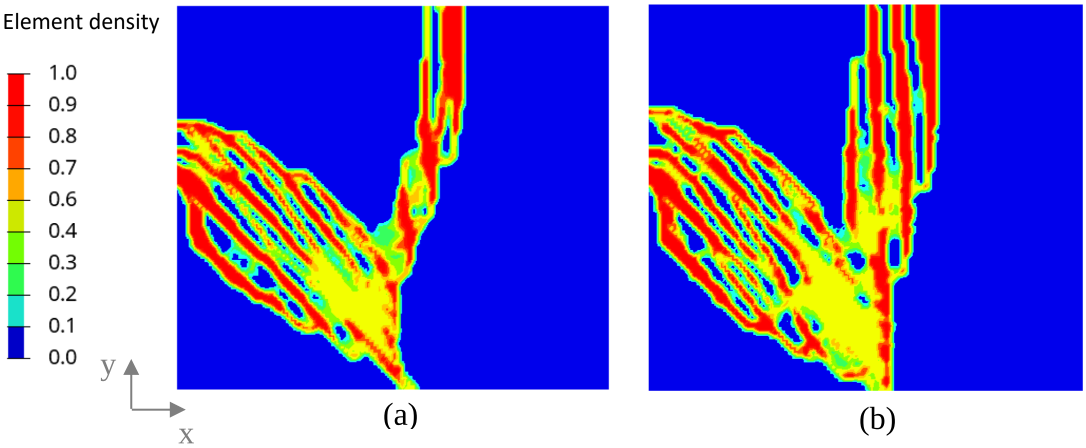

Figure A.4. Element density plot for the reference model under load case 1 for a remaining Area of (a) 15 % and (b) 20 %

A.5 3D view of the rib model

An additional view of the rib model is given in Figure A.5.

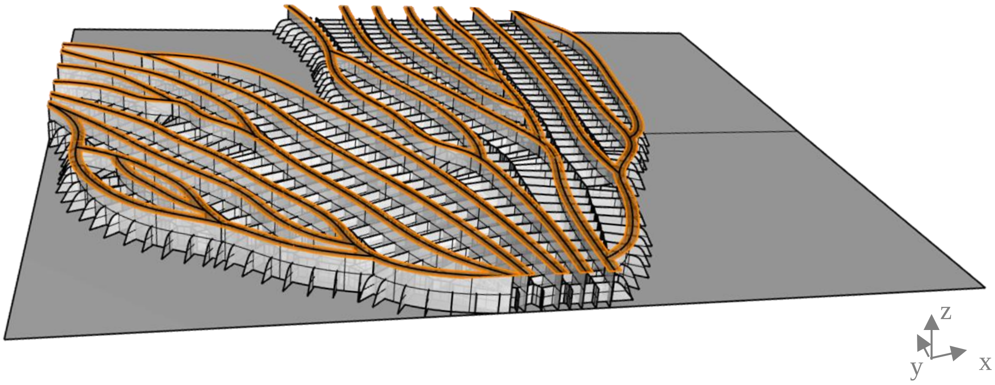

Figure A.5. 3D view of the rib model. The sandwich structure is indicated in orange.

A.6 Combined model without thickness optimisation

Figure A.6 shows the overall displacement of the combined model with $\delta_{max} = 5.68\,mm$, before performing a thickness optimisation. The base plate has $t = 1\,mm$ and the stiffening structures have $t = 1.2\,mm$.

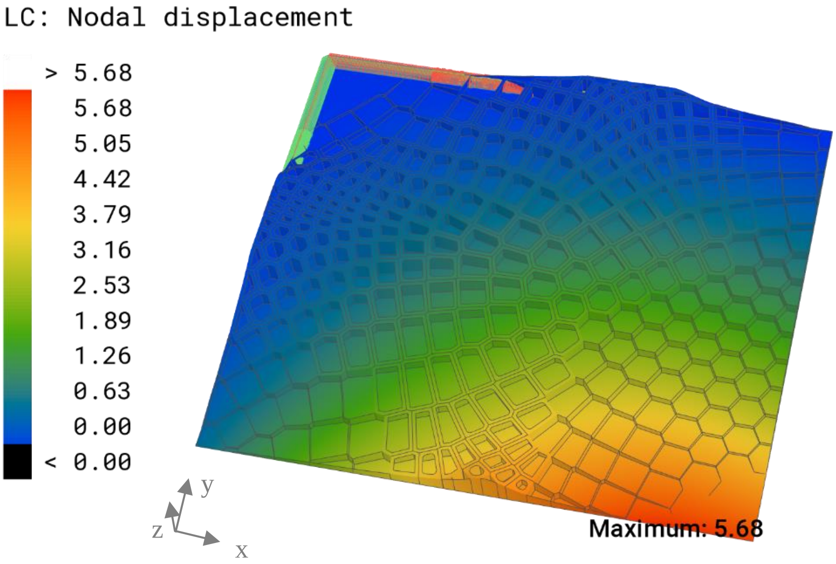

Figure A.6. Overall displacement plot and maximum overall displacement [mm] of the combined model without a thickness optimisation.